

A TEST OF THE MILLISECOND MAGNETAR CENTRAL ENGINE MODEL OF GRBS WITH SWIFT DATA

HOU-JUN LÜ, BING ZHANG

Department of Physics and Astronomy, University of Nevada Las Vegas, Las Vegas, NV 89154, USA
lhj@physics.unlv.edu, zhang@physics.unlv.edu

ABSTRACT

A rapidly spinning, strongly magnetized neutron star (magnetar) has been proposed as one possible candidate of the central engine of gamma-ray bursts (GRBs). We systematically analyze the Swift/XRT light curves of long GRBs detected before 2013 August, and characterize them into four categories based on how likely they may harbor a magnetar central engine: Gold, Silver, Aluminum, and Non-magnetar. We also independently analyze the data of short GRBs with a putative magnetar central engine. We then perform a statistical study of various properties of the magnetar samples and the non-magnetar sample, and investigate whether the data are consistent with the hypothesis that there exist two types of central engines. By deriving the physical parameters of the putative magnetars, we find that the observations of the Gold and Silver samples are generally consistent with the predictions of the magnetar model. For a reasonable beaming factor for long GRBs, the derived magnetar surface magnetic field B_p and initial spin period P_0 fall into the reasonable range. Magnetar winds in short GRBs, on the other hand, are consistent with being isotropic. No GRB in the magnetar sample has a beam-corrected total energy exceeding the maximum energy budget defined by the initial spin energy of the magnetar, while some non-magnetar GRBs do violate such a limit. With beaming correction, on average the non-magnetar sample is more energetic and luminous than the magnetar samples. Our analysis hints that millisecond magnetars are likely operating in a good fraction, but probably not all, GRBs.

Subject headings: gamma-rays: bursts: methods: statistical: radiation mechanisms: non-thermal

1. INTRODUCTION

The central engine of gamma-ray bursts (GRBs) remains an open question in GRB physics (Zhang 2011). Observations of GRB prompt emission and early afterglow pose the following constraints on a successful central engine model: (1) The central engine must be able to power an outflow with an extremely high energy and luminosity (e.g. Zhang & Mészáros, 2004; Meszaros 2006); (2) The ejecta must have a low baryon loading, with energy per baryon exceeding 100 (e.g. Lithwick & Sari, 2001; Liang et al. 2010); (3) The central engine should be intermittent in nature to account for the observed light curves with rapid variability (Fishman & Meagan 1995); (4) The engine should last for an extended period of time to power delayed erratic X-ray flares (Burrows et al. 2005; Zhang et al. 2006) or long-lasting X-ray emission followed by a sudden drop (i.e. “internal plateau”, Troja et al. 2007; Liang et al. 2007; Lyons et al. 2010); (5) Finally, Fermi observations require that the central engine should be strongly magnetized to launch a magnetically dominated outflow at least for some GRBs (Zhang & Pe’er 2009).

Two types of GRB central engine models have been discussed in the literature (e.g. Kumar & Zhang 2014 for a review). The leading type of models invokes a hyper-accreting stellar-mass black hole (e.g. Popham et al. 1999; Narayan et al. 2001; Lei et al. 2013), from which a relativistic jet is launched via neutrino-anti-neutrino annihilation (Ruffert et al. 1997; Popham et al. 1999; Chen & Beloborodov 2007; Lei et al. 2009), Blandford-Znajek mechanism (Blandford & Znajek 1977; Lee et al. 2000; Li 2000), or episodic magnetic bubble ejection from the disk (Yuan & Zhang 2012).

The second type of models invokes a rapidly spinning,

strongly magnetized neutron star dubbed a “millisecond magnetar” (Usov 1992; Thompson 1994; Dai & Lu 1998a; Wheeler et al. 2000; Zhang & Mészáros 2001; Metzger et al. 2008, 2011; Bucciantini et al. 2012). Within this scenario, the energy reservoir is the total rotation energy of the millisecond magnetar, which reads

$$E_{\text{rot}} = \frac{1}{2} I \Omega_0^2 \simeq 2 \times 10^{52} \text{ erg } M_{1.4} R_6^2 P_{0,-3}^{-2}, \quad (1)$$

where I is the moment of inertia, $\Omega_0 = 2\pi/P_0$ is the initial angular frequency of the neutron star, $M_{1.4} = M/1.4M_\odot$, and the convention $Q = 10^Q Q_x$ is adopted in cgs units for all other parameters throughout the paper.

Assuming that the magnetar with initial spin period P_0 is being spun down by a magnetic dipole with surface polar cap magnetic field B_p , the spindown luminosity would evolve with time as (Zhang & Mészáros 2001)

$$L(t) = L_0 \frac{1}{(1 + t/\tau)^2} \simeq \begin{cases} L_0, & t \ll \tau, \\ L_0(t/\tau)^{-2}, & t \gg \tau. \end{cases} \quad (2)$$

where

$$L_0 = 1.0 \times 10^{49} \text{ erg s}^{-1} (B_{p,15}^2 P_{0,-3}^{-4} R_6^6) \quad (3)$$

is the characteristic spindown luminosity, and

$$\tau = 2.05 \times 10^3 \text{ s } (I_{45} B_{p,15}^{-2} P_{0,-3}^2 R_6^{-6}) \quad (4)$$

is the characteristic spindown time scale.

The spin-down behavior of the magnetar can leave characteristic imprints in the observed GRB emission.

Dai & Lu (1998a) first proposed an energy injection model of millisecond pulsars to interpret a rebrightening feature of the first optical afterglow detected in GRB 970228. The required B_p is $\sim 10^{13}$ G, not quite a magnetar strength. The prompt GRB emission has to be attributed to additional physical processes, e.g. magnetic dissipation in a differentially rotating neutron star (Kluźniak & Ruderman 1998) or strange quark star (Dai & Lu 1998b). Zhang & Mészáros (2001) studied energy injection from a central engine with a general luminosity law $L(t) = L_0(t/t_0)^{-q}$ (the magnetar injection corresponds to $q = 0$ for $t < \tau$ and $q = 2$ for $t > \tau$), and pointed out that besides the rebrightening feature discussed by Dai & Lu (1998a,b), for more typical magnetar parameters, one can have a shallow decay phase followed by a normal decay phase in the early afterglow of a GRB. Such a shallow decay phase (or plateau) was later commonly observed in Swift early XRT light curves (Zhang et al. 2006; Nousek et al. 2006; O’Brien et al. 2006; Liang et al. 2007). It can be readily interpreted as energy injection from a millisecond magnetar central engine (Zhang et al. 2006). An alternative energy injection model invokes a short-duration central engine, which ejects materials with a stratified Lorentz factor (Γ) profile. Energy is gradually added to the blastwave as the blastwave is gradually decelerated to progressively lower Γ (Rees & Mészáros 1998; Sari & Mészáros 2000; Uhm et al. 2012). Both models can interpret the shallow decay phase of most X-ray light curves.

A tie-breaker GRB was discovered in early 2007. GRB 070110 (Troja et al. 2007) showed an extended plateau with a near flat light curve extending to over 10^4 seconds before rapidly falling off with a decay index $\alpha \sim 9$ (throughout the paper the convention $F_\nu \propto t^{-\alpha}\nu^{-\beta}$ is adopted). Such a rapid decay cannot be accommodated in any external shock model, so that the entire X-ray plateau emission has to be attributed to internal dissipation of a central engine wind. Such an “internal plateau” was later discovered in several more GRBs (Liang et al. 2007; Lyons et al. 2010). The near steady X-ray emission observed in GRB 070110 may not be easy to interpret within a black hole central engine model, but is a natural prediction of the magnetar central engine model (Eq.(2) when $t \ll \tau$). The rapid t^{-9} decay near the end is not predicted in the magnetic dipole radiation model. Troja et al. (2007) interpreted it as being due to collapse of the magnetar to a black hole after loosing centrifugal support¹. Interestingly, internal plateaus are also discovered in a good fraction of short GRBs (Rowlinson et al. 2010, 2013). Modeling various afterglow features for both long and short GRBs within the framework of the millisecond magnetar (or pulsar with weaker magnetic field) central engine model has gained growing attention (Dai et al. 2006; Gao & Fan 2006; Fan & Xu 2006; Metzger et al. 2008, 2011; Dall’Osso et al. 2011; Fan et al. 2011; Bucciantini et al. 2012; Bernardini et al.

2013; Gompertz et al. 2013, 2014). Numerical simulations of binary neutron star mergers indeed show that a stable magnetar can survive if the initial masses of the two neutron stars are small enough, which would power a short gamma-ray burst (Giacomazzo & Perna. 2013).

Even though evidence of a magnetar central engine is mounting, it remains unclear whether the rich GRB data accumulated over the years with the GRB mission Swift indeed statistically requires the existence of (presumably) two types of central engines. If indeed magnetars are operating in some GRBs while hyper-accreting black holes are operating in others, do the data show statistically significant differences between the two samples? Do those GRBs that seem to have a magnetar signature have physical parameters that are consistent with the predictions of the magnetar central engine model?

This paper is to address these interesting questions through a systematic analysis of the Swift X-Ray Telescope (XRT) data. The XRT data reduction details and criteria for sample selection are presented in §2. In §3, physical parameters of the GRBs and the hypothetical magnetars are derived for all the samples. A statistical comparison of the physical properties between the magnetar samples and the non-magnetar sample are presented in §4, and conclusions are drawn in §5 with some discussion. Throughout the paper, a concordance cosmology with parameters $H_0 = 71 \text{ km s}^{-1} \text{ Mpc}^{-1}$, $\Omega_M = 0.30$, and $\Omega_\Lambda = 0.70$ is adopted.

2. DATA REDUCTION AND SAMPLE SELECTION CRITERIA

The XRT data are downloaded from the Swift data archive². We developed a script to automatically download and maintain all the XRT data on the local UNLV machine. The HEASoft packages *version 6.10*, including Xspec, Xselect, Ximage, and the Swift data analysis tools, are used for the data reduction. An IDL code was developed by the former group member B.-B. Zhang to automatically process the XRT data for a given burst in any user-specified time interval (see Zhang et al. 2007c for details). We adopt this code with slight modifications to solve the problem designed for this paper. The same IDL code was used in several previous papers (Zhang et al. 2007c; Liang et al. 2007, 2008, 2009) of our group. More details about the data reduction procedures can be found in Zhang et al. (2007c) and Evans et al. (2009).

Our entire sample includes more than 750 GRBs observed between 2005 January and 2013 August, whose XRT data are all processed with our data reduction tool. Since the magnetar signature typically invokes a shallow decay phase (or plateau) followed by a steeper decay segment (a normal decay for canonical light curves, or a very steep decay for internal plateaus), our attention is on those GRBs that show such a transition in the X-ray light curves. We first identify such bursts by inspecting their light curves. In order to grade their magnetar candidacy, we next perform a temporal fit to the plateau behavior within a time interval (t_1, t_2) , where t_1 is the beginning of the plateau, while t_2 is the end of the segment after the plateau break (either last observed data point if there is no further break in the lightcurve, or the break time if a second break appears). Since we are mostly

¹ Such an interpretation recently gains indirect support. Zhang (2014) suggested that such an implosion in the GRB early afterglow phase should be accompanied by a fast radio burst (FRB) (see also Falcke & Rezzolla 2013 for a proposal of more general supra-massive neutron star implosions as the sources of FRBs), and tentative detections of these FRBs following two GRBs may have been detected (Bannister et al. 2012), roughly around the time suggested by Zhang (2014).

² <http://www.swift.ac.uk/archive/obs.php?burst=1>

interested in the behavior around the break time t_b , the exact positions of t_1 and t_2 do not matter much, so we pick them through visual inspection of the light curves. We then fit the light curves with a smooth broken power law

$$F = F_0 \left[\left(\frac{t}{t_b} \right)^{\omega\alpha_1} + \left(\frac{t}{t_b} \right)^{\omega\alpha_2} \right]^{-1/\omega}, \quad (5)$$

where t_b is the break time, $F_b = F_0 \cdot 2^{-1/\omega}$ is the flux at the break time t_b , α_1 and α_2 are decay indices before and after the break, respectively, and ω describes the sharpness of the break. The larger the ω parameter, the sharper the break.

An IDL routine named “mpfitfun.pro” is employed for our fitting (Moré 1977; Markwardt 2009). This routine performs a Levenberg-Marquardt least-square fit to the data for a given model to optimize the model parameters. After processing all the data, we grade all long GRBs in our sample into four groups (“Gold”, “Silver”, “Aluminum”, and “non-magnetar”) according to their likelihood of being powered by a magnetar central engine.

- **Gold:** This sample is defined by those bursts that display an “internal plateau”. These plateaus are followed by a decay slope steeper than 3, which is essentially impossible to interpret within the external shock models (Gao et al. 2013b)³. It demands a long-lasting central engine, and a near steady flux is consistent with emission from a spinning down magnetar. The rapid decay at the end of plateau may mark the implosion of the magnetar into a black hole (Troja et al. 2007; Zhang 2014). There are altogether only 9 robust cases identified in this Gold sample, 3 of which have redshift measurements. The light curves of these 9 GRBs together with the broken power-law fittings (red curves) are shown in Figure 1, and the fitting parameters are summarized in Table 1.
- **Silver:** This sample includes GRBs with a shallow decay phase followed by a normal decay phase, and the pre- and post-break temporal and spectral properties are well consistent with the external forward shock model with energy injection of a magnetar as defined in Eq.(2). Specifically, one requires two independent criteria to define this sample. First, the temporal and spectral properties of the afterglow after the break (the normal decay phase) should satisfy the “closure relation” of the external shock model (e.g. Zhang & Mészáros 2004; Gao et al. 2013b), i.e.

$$\alpha_2 = \begin{cases} \frac{3\beta}{2} = \frac{3(p-1)}{4}, & \nu_m < \nu < \nu_c \text{ (ISM)} \\ \frac{3\beta+1}{2} = \frac{3p-1}{4}, & \nu_m < \nu < \nu_c \text{ (Wind)} \\ \frac{3\beta-1}{2} = \frac{3p-2}{4}, & \nu > \nu_c \text{ (ISM or Wind)} \end{cases} \quad (6)$$

Here β is the spectral index of the normal decay segment (which is X-ray photon index minus 1),

³ The steepest decay slope in an external shock model is $2 + \beta$ (Kumar & Panaitescu 2000), which is typically smaller than 3, and is defined by the high-latitude “curvature effect” emission from a conical outflow, even if the emission abruptly ceases.

and p is the electron’s spectral distribution index. Second, the pre-break slope α_1 should correspond to $q = 0$, while the post-break slope α_2 should correspond to $q = 1$ (for a constant energy fireball, the scaling law is the same as $q = 1$, Zhang & Mészáros 2001), so according to Zhang et al. (2006) and Gao et al. (2013b), one should have

$$\alpha_1 = \begin{cases} \frac{2\alpha_2-3}{3}, & \nu_m < \nu < \nu_c \text{ (ISM)} \\ \frac{2\alpha_2-1}{3}, & \nu_m < \nu < \nu_c \text{ (Wind)} \\ \frac{2\alpha_2-2}{3}, & \nu > \nu_c \text{ (ISM or Wind)} \end{cases} \quad (7)$$

In our entire sample, 69 GRBs can be grouped into this Silver sample, with 33 having measured redshifts. The light curves with fitting curves are presented online at [http://grb.physics.unlv.edu/\\$\sim\\$lhj/Silver/](http://grb.physics.unlv.edu/\simlhj/Silver/), and the fitting results are reported in Table 1. Two examples (GRBs 060729, see also Grupe et al. 2007, and 070306) are shown in Figure 2. Figure 3 shows all the GRBs in the $\alpha_1 - \alpha_2$ plane, with three theoretically favored lines of the magnetar models (Eq.(7)) plotted. Those GRBs falling onto these lines (within error bars) and also satisfy the closure relations are identified as Silver sample GRBs (colored data points). In Fig.4 we present the distribution of electron spectral index p derived from the Silver sample. It has a Gaussian distribution with a center value $p_c = 2.51 \pm 0.04$. Figure 5 shows the distribution of Silver sample in the (α, β) -plane combined with the closure relations for the models (ISM and wind medium).

- **Aluminum:** Other GRBs with a shallow decay segment transiting to a steeper decay are included in the Aluminum sample. They either do not satisfy external shock closure relations in the post-break phase, or do not satisfy the $\alpha_1 - \alpha_2$ relations predicted in the magnetar external shock models. These are marked as grey points in Fig.3. Those GRBs that fall onto the three magnetar model lines but are still denoted as Aluminum are the ones that do not satisfy the closure relations in the post-break phase. On the other hand, since early magnetar spindown may not fully follow the simple dipole spindown law (e.g. Metzger et al. 2011), and since the observed X-ray emission may not come from the external forward shock emission (e.g. can be from external reverse shock, Dai 2004; Yu & Dai 2007, or from internal dissipation of the magnetar wind, Yu et al. 2010), these GRBs could be still powered by magnetars. We therefore still assign them as magnetar candidates, but with a lower grade. There are 135 solid cases in the sample, 67 of which have redshift measurements. The light curves with fitting curves are presented online at [http://grb.physics.unlv.edu/\\$\sim\\$lhj/Aluminum/](http://grb.physics.unlv.edu/\simlhj/Aluminum/). Two examples (GRBs 070420 and 080430) are presented in Fig.2.
- **Non-magnetar:** All the other long GRBs we have analyzed are included in the non-magnetar sample. They either have a single power-law decay, or

have erratic flares that prevent identifying a clear shallow decay phase, or present a rebrightening behavior, or the data are too poor to reach a robust conclusion. There are more than 400 GRBs in this group, 111 of which have redshift measurements. Strictly speaking, some of these GRBs may still host a magnetar central engine. We define these GRBs as “non-magnetar”, simply because they do not present a clear magnetar signature. Two examples (GRBs 061007, see also Schady et al. 2007, Mundell et al. 2007, and 081028) are presented in the Fig. 2.

Finally, we also independently processed the X-ray data of short GRBs that may harbor a magnetar central engine (cf. Rowlinson et al. 2013). We select the short GRBs that have measured redshifts and high-quality X-ray data. The light curves with fitting curves are presented online at [http://grb.physics.unlv.edu/\\$\sim\\$hlhj/SGRB/](http://grb.physics.unlv.edu/\simhlhj/SGRB/).

3. DERIVATIONS OF THE PHYSICAL PARAMETERS

Our purpose is to analyze and compare the physical properties of GRBs with or without a magnetar signature. In this section, we use data to derive relevant physical parameters. Redshift measurements are crucial to derive the intrinsic parameters (energy, luminosity, etc), so in the following we focus on those GRBs with z measurements only.

3.1. Energetics, luminosity, and radiation efficiency

The isotropic prompt γ -ray emission energy $E_{\gamma, \text{iso}}$ is usually derived from the observed fluence S_γ in the detector’s energy band, and extrapolated to the rest-frame $1-10^4$ keV using spectral parameters (the low- and high-energy spectral indices $\hat{\alpha}$, $\hat{\beta}$, and the peak energy E_p for a standard “Band-function” fit, Band et al. 1993) and through k -correction. However, since the BAT energy band is narrow (15-150 keV), for most GRBs the spectra can be only fit by a cutoff power law or a single power law (Sakamoto et al. 2008, 2011). We therefore apply the following procedure to estimate the Band spectral parameters: (1) If a burst was also detected by *Fermi* GBM or *Konus* Wind, we adopt the spectral parameters measured by those instruments. (2) For those bursts that are not detected by other instruments but can be fit with a cutoff power law model, we adopt the derived $\hat{\alpha}$ and E_p parameters⁴, and assume a typical value of $\hat{\beta} = -2.3$. (3) For those GRBs that can be only fit with a single power law, we have to derive E_p using an empirical correlation between the BAT-band photon index Γ^{BAT} and E_p (e.g. Sakamoto et al. 2009; Zhang et al. 2007b; Virgili et al. 2012; Lü et al. 2012). The typical parameters $\hat{\alpha} = -1$, $\hat{\beta} = -2.3$ are adopted to perform the simulations. We can then calculate the $E_{\gamma, \text{iso}}$ according to

$$\begin{aligned} E_{\gamma, \text{iso}} &= 4\pi k D_L^2 S_\gamma (1+z)^{-1} \\ &= 1.3 \times 10^{51} \text{ erg } k D_{28}^2 (1+z)^{-1} S_{\gamma, -6} \end{aligned} \quad (8)$$

⁴ We note that usually the low-energy photon index $\hat{\alpha}$ and E_p are slightly different for the cut-off power law and Band-function models (e.g. Sakamoto et al. 2008, 2011), but the derived $E_{\gamma, \text{iso}}$ only shows a slight difference, which is ignored in our analysis.

where z is the redshift, $D = 10^{28}$ cm D_{28} is the luminosity distance, and k is the k -correction factor from the observed band to $1-10^4$ keV in the burst rest frame (e.g. Bloom et al. 2001).

Another important parameter is the isotropic kinetic energy $E_{K, \text{iso}}$ measured from the afterglow flux. This value is increasing during the shallow decay phase, but becomes constant during the normal decay phase (Zhang et al. 2007a). We follow the method discussed in Zhang et al. (2007a) to calculate $E_{K, \text{iso}}$ during the normal decay phase using the X-ray data. Noticing that fast-cooling is disfavored at this late epoch, we derive several relevant cases. For $\nu > \max(\nu_m, \nu_c)$, the afterglow flux expression does not depend on the medium density, so the following expression (Zhang et al. 2007a) applies to both ISM and wind models⁵

$$\begin{aligned} E_{K, \text{iso}, 52} &= \left[\frac{\nu F_\nu(\nu = 10^{18} \text{ Hz})}{5.2 \times 10^{-14} \text{ ergs s}^{-1} \text{ cm}^{-2}} \right]^{4/(p+2)} \\ &\times D_{28}^{8/(p+2)} (1+z)^{-1} t_d^{(3p-2)/(p+2)} \\ &\times (1+Y)^{4/(p+2)} f_p^{-4/(p+2)} \epsilon_{B, -2}^{(2-p)/(p+2)} \\ &\times \epsilon_{e, -1}^{4(1-p)/(p+2)} \nu_{18}^{2(p-2)/(p+2)}. \end{aligned} \quad (9)$$

For the $\nu_m < \nu < \nu_c$ ISM model, one has (Zhang et al. 2007a)

$$\begin{aligned} E_{K, \text{iso}, 52} &= \left[\frac{\nu F_\nu(\nu = 10^{18} \text{ Hz})}{6.5 \times 10^{-13} \text{ ergs s}^{-1} \text{ cm}^{-2}} \right]^{4/(p+3)} \\ &\times D_{28}^{8/(p+3)} (1+z)^{-1} t_d^{3(p-1)/(p+3)} \\ &\times f_p^{-4/(p+3)} \epsilon_{B, -2}^{-(p+1)/(p+3)} \epsilon_{e, -1}^{4(1-p)/(p+3)} \\ &\times n^{-2/(p+3)} \nu_{18}^{2(p-3)/(p+3)}. \end{aligned} \quad (10)$$

For the $\nu_m < \nu < \nu_c$ wind model, one has (Gao et al. 2013b)

$$\nu_m = 5.5 \times 10^{11} \text{ Hz} \left(\frac{p-2}{p-1} \right)^2 (1+z)^{1/2} \epsilon_{B, -2}^{1/2} \epsilon_{e, -1}^2 E_{K, \text{iso}, 52}^{1/2} t_d^{-3/2}, \quad (11)$$

$$\nu_c = 4.7 \times 10^{18} \text{ Hz} (1+z)^{-3/2} A_{*, -1}^{-2} \epsilon_{B, -2}^{-3/2} E_{K, \text{iso}, 52}^{1/2} t_d^{1/2}, \quad (12)$$

$$F_{\nu, \text{max}} = 5.7 \times 10^2 \mu \text{ Jy} (1+z)^{3/2} A_{*, -1}^{1/2} \epsilon_{B, -2}^{-2} D_{28}^{-2} E_{K, \text{iso}, 52}^{1/2} t_d^{-1/2}, \quad (13)$$

so that

$$\begin{aligned} \nu F_\nu(\nu = 10^{18} \text{ Hz}) &= \nu F_{\nu, \text{max}} \left(\frac{\nu}{\nu_m} \right)^{-(p-1)/2} \\ &= F_{\nu, \text{max}} \nu^{(3-p)/2} \nu_m^{(p-1)/2} \end{aligned}$$

⁵ The coefficients may be slightly different for the two ambient medium models. Since in this regime one cannot differentiate the two circumburst medium models, we universally adopt this equation derived from the ISM model, keeping in mind that there might be a factor of a few correction if the medium is wind-like.

$$\begin{aligned}
&= 7.4 \times 10^{-14} \text{ erg cm}^{-2} \text{ s}^{-1} \\
&\times D_{28}^{-2} (1+z)^{(p+5)/4} A_{*, -1} f_p \epsilon_{B, -2}^{(p+1)/4} \epsilon_{e, -1}^{p-1} \\
&\times E_{K, \text{iso}, 52}^{(p+1)/4} t_d^{(1-3p)/4} \nu_{18}^{(3-p)/2}, \quad (14)
\end{aligned}$$

and

$$\begin{aligned}
E_{K, \text{iso}, 52} &= \left[\frac{\nu F_\nu(\nu = 10^{18} \text{ Hz})}{7.4 \times 10^{-14} \text{ ergs s}^{-1} \text{ cm}^{-2}} \right]^{4/(p+1)} \\
&\times D_{28}^{8/(p+1)} (1+z)^{-(p+5)/(p+1)} t_d^{(3p-1)/(p+1)} \\
&\times f_p^{-4/(p+1)} \epsilon_{B, -2}^{-1} \epsilon_{e, -1}^{4(1-p)/(p+1)} \\
&\times A_{*, -1}^{-4/(p+1)} \nu_{18}^{2(p-3)/(p+1)}. \quad (15)
\end{aligned}$$

Here $\nu f_\nu(\nu = 10^{18} \text{ Hz})$ is the energy flux at 10^{18} Hz (in units of $\text{ergs s}^{-1} \text{ cm}^{-2}$), n is the density of the constant ambient medium, A_* is the stellar wind parameter, t_d is the time in the observer frame in days, and Y is the Compton parameter. The electron spectral index p and the spectral index β are connected through

$$p = \begin{cases} 2\beta + 1, & \nu_m < \nu < \nu_c \\ 2\beta, & \nu > \nu_c, \end{cases} \quad (16)$$

and f_p is a function of the power law distribution index p (Zhang et al. 2007a)

$$f_p \sim 6.73 \left(\frac{p-2}{p-1} \right)^{p-1} (3.3 \times 10^{-6})^{(p-2.3)/2} \quad (17)$$

In our calculations, the microphysics parameters of the shock are assigned to standard values derived from observations (e.g. Panaitescu & Kumar 2002; Yost et al. 2003): $\epsilon_e = 0.1$ and $\epsilon_B = 0.01$. The Compton parameter is assigned to a typical value $Y = 1$.

After deriving the break time t_b through light curve fitting, we derive the break time luminosity as

$$L_b = 4\pi D^2 F_b, \quad (18)$$

where F_b is the X-ray flux at t_b . Since the XRT band is narrow, no k -correction is possible to calculate L_b .

A jet break was detected in some GRBs in our sample. For these GRBs, we correct all the isotropic values to the beaming-corrected values by multiplying the values by the beaming correction factor (Frail et al. 2001)

$$f_b = 1 - \cos \theta_j \simeq (1/2) \theta_j^2, \quad (19)$$

i.e. $E_\gamma = E_{\gamma, \text{iso}} f_b$, and $E_K = E_{K, \text{iso}} f_b$. The jet angle information was searched from the literature (e.g. Liang et al. 2008; Racusin et al. 2009; Lu et al. 2012; Nemmen et al. 2012), which is collected in Table 2.

The GRB radiation efficiency is defined as (Lloyd-Ronning & Zhang 2004)

$$\eta_\gamma = \frac{E_{\gamma, \text{iso}}}{E_{\gamma, \text{iso}} + E_{K, \text{iso}}} = \frac{E_\gamma}{E_\gamma + E_K}. \quad (20)$$

Since $E_{K, \text{iso}}$ (and E_K) are increasing functions of time during the shallow decay phase, η_γ is different when $E_{K, \text{iso}}$ (E_K) at different epochs are adopted. Following Zhang et al. (2007a), we take a typical blastwave deceleration t_{dec} and the end of the shallow decay phase t_b to calculate the radiative efficiencies. Within the framework

of the magnetar central engine model, the two efficiencies carry different physical meanings: $\eta_\gamma(t_{\text{dec}})$ denotes the efficiency of dissipating the magnetar wind energy during the prompt emission phase, while $\eta_\gamma(t_b)$ denotes the total efficiency of converting the spindown energy of a magnetar to γ -ray radiation.

3.2. Magnetar parameters

For a magnetar undergoing dipolar spindown, two important magnetar parameters, i.e. the initial spin period P_0 and the surface polar cap magnetic field B_p , can be solved by the characteristic luminosity L_0 (Eq.(3)) and the spindown time scale τ (Eq.(4)).

The spindown time scale can be generally identified as the observed break time, i.e.

$$\tau = t_b / (1+z). \quad (21)$$

One caution is that τ can be shorter than $t_b / (1+z)$ if the magnetar is supra-massive, and collapses to a black hole before it is significantly spun down. On the other hand, the angular velocity of the magnetar does not change significantly until reaching the characteristic spindown time scale, so that the collapse of the supra-massive magnetar, if indeed happens, would likely happen at or after τ . In our analysis, we will adopt Eq.(21) throughout.

The characteristic spindown luminosity should generally include two terms:

$$L_0 = L_X + L_K = (L_{X, \text{iso}} + L_{K, \text{iso}}) f_b, \quad (22)$$

where $L_{X, \text{iso}}$ is the X-ray luminosity due to internal dissipation of the magnetar wind, which is the observed X-ray luminosity of the internal plateau (for external plateaus, one can only derive an upper limit), and

$$L_{K, \text{iso}} = E_{K, \text{iso}} (1+z) / t_b \quad (23)$$

is the kinetic luminosity that is injected into the blast-wave during the energy injection phase. It depends on the isotropic kinetic energy $E_{K, \text{iso}}$ after the injection phase is over, which can be derived from afterglow modeling discussed above. For the Gold sample, the $L_{X, \text{iso}}$ component dominates, while for Silver and Aluminum samples, the $L_{K, \text{iso}}$ component dominates. In any case, both components should exist and contribute to the observed flux (Zhang 2014). One can also define an X-ray efficiency to define the radiative efficiency for a magnetar to convert its spindown energy to radiation, i.e.

$$\eta_X = \frac{L_X}{L_X + L_K} = \frac{L_{X, \text{iso}}}{L_{X, \text{iso}} + L_{K, \text{iso}}}. \quad (24)$$

In our analysis, we try to calculate both $L_{X, \text{iso}}$ and $L_{K, \text{iso}}$ from the data. For the Gold sample GRBs that show internal plateaus, $L_{X, \text{iso}}$ can be readily measured. For the cases where the internal plateau lands on an external shock component (e.g. Troja et al. 2007), $L_{K, \text{iso}}$ can be also derived by modeling the late X-ray afterglow in the normal decay phase. For the Gold sample cases where no late external shock component is available, one can only set up an upper limit on $L_{K, \text{iso}}$. For Silver and Aluminum samples, the internal plateau component is not detectable. Through simulations, we find that the external shock component would not be significantly modified if the internal plateau flux is below 50% of the observed external shock flux. Therefore for all the

Silver and Aluminum sample GRBs, we place an upper limit of $L_{X,\text{iso}}$ as 50% of the observed X-ray flux.

4. RESULTS

4.1. Magnetar parameters and collimation

We derive magnetar parameters (P_0 and B_p) of the Gold, Silver and Aluminum samples using Eqs.(3), (4), and (22)⁶. First, we assume that the magnetar wind is isotropic, so that $f_b = 1$. The derived P_0 , B_p are presented in Table 2 and Fig.6a. Most “magnetars” have B_p below 10^{15} G, some even have B_p below 10^{13} G, which are not considered as magnetars. More problematically, most derived P_0 ’s are much shorter than 1 ms. This directly conflicts with the break-up limit of a neutron star, which is about 0.96 ms (Lattimer & Prakash 2004). This suggests that the isotropic assumption for these long GRB magnetar winds is not correct. We then introduce the beaming factor f_b for each GRB. If θ_j is measured, we simply adopt the value. Otherwise, we choose $\theta_j = 5^\circ$, a typical jet opening angle for bright long GRBs (Frail et al. 2001; Liang et al. 2008). Very interestingly, after such a correction, all the data points of Gold and Silver sample GRBs fall into the expected region in the $P_0 - B_p$ plot (Fig.6b). Also the additional conditions imposed by the causality argument (i.e. that the speed of sound on the neutron star cannot exceed the speed of light, Lattimer et al. 1990, and Eqs.(9) and (10) of Rowlinson et al. (2010)) are satisfied for all GRBs in all three (Gold, Silver and Aluminum) magnetar samples, if one assumes $M = 1.4M_\odot$. All these suggest that the long GRB magnetar winds are likely collimated. Some Aluminum sample GRBs are still to the left of the allowed region (with P_0 shorter than the break-up limit). This may suggest that those Aluminum sample bursts are not powered by magnetars, or are powered by magnetars with even narrower jets.

Very interestingly, the magnetar properties of short GRBs derived under the isotropic assumption actually lie reasonably in the allowed region (Fig.6a, blue dots). After jet correction for long GRB magnetars (but keep short GRB magnetar wind isotropic), the derived magnetar parameters are well mixed in the same region. This suggests that the isotropic assumption for short GRBs is reasonably good. This is understandable within the framework of the progenitor models of GRBs. Short GRBs are believed to be powered by mergers of NS-NS or NS-BH systems (Paczynski 1986; Eichler et al. 1989; Paczynski 1991; Narayan et al. 1992). During the merger process, only a small amount of materials are launched (Freiburghaus et al. 1999; Rezzolla et al. 2010; Hotokezaka et al. 2013). A millisecond magnetar is expected to launch a near isotropic wind. This wind, instead of being collimated by the ejecta (e.g. Bucciantini et al. 2012), would simply push the ejecta behind and accelerate the ejecta and make a bright electromagnetic signal in the equatorial directions (Fan & Xu 2006; Zhang

2013; Gao et al. 2013; Yu et al. 2013; Metzger & Piro 2013). In the jet direction, the magnetar wind emission is not enhanced by the beaming effect, so that one can infer correct magnetar parameters assuming an isotropic wind. For long GRBs, on the other hand, jets are believed to be launched from collapsing massive stars (Woosley 1993; MacFadyen & Woosley 1999). The initially near isotropic magnetar wind is expected to be soon collimated by the stellar envelope to a small solid angle (Bucciantini et al. 2008).

4.2. Statistical properties and correlations of other parameters

Figure 7 shows the correlations of $L_b - E_{\gamma,\text{iso}}$ and $L_b - t_b$ for the entire sample. As shown in Fig.7a, a higher isotropic γ -ray energy generally has a higher X-ray break luminosity. For the Gold and Silver samples, a Spearman correlation analysis gives a dependence

$$\log L_{b,49} = (1.48 \pm 0.17) \log E_{\gamma,\text{iso},52} + (2.56 \pm 0.75), \quad (25)$$

with a correlation coefficient $r = 0.83$, and a chance probability $p < 0.001$. Adding the Aluminum sample only slightly worsens the correlation ($\log L_{b,49} = (1.02 \pm 0.10) \log E_{\gamma,\text{iso},52} + (2.64 \pm 2.04)$, with $r = 0.72$ and $p < 0.001$). Such a correlation is expected, which may be caused by a combination of intrinsic (a more energetic magnetar gives more significant contribution to both prompt emission and afterglow) and geometric effects (a narrower jet would enhance both prompt emission and afterglow).

Figure 7b presents an anti-correlation between L_b and t_b (Dainotti et al. 2010). Our Gold + Silver sample gives

$$\log L_{b,49} = (-1.83 \pm 0.20) \log t_{b,3} + (0.2 \pm 0.18) \quad (26)$$

with $r = 0.84$ and $p < 0.001$. Adding the Aluminum sample only slightly worsens the correlation ($\log L_{b,49} = (-1.29 \pm 0.15) \log t_{b,3} - (0.43 \pm 0.14)$ with $r = 0.66$ and $p < 0.001$). Such an anti-correlation is consistent with the prediction of the magnetar model: Given a quasi-universal magnetar total spin energy, a higher magnetic field would power a brighter plateau with a shorter duration, or vice versa (see also Xu & Huang 2012).

In Fig.8, we compare the inferred $E_\gamma + E_K$ with the total rotation energy E_{rot} (Eq.(1)) of the millisecond magnetar. It is found that the GRBs are generally above and not too far above the $E_{\text{rot}} = E_\gamma + E_K$ line. This is consistent with the magnetar hypothesis, namely, all the emission energy ultimately comes from the spin energy of the magnetar. Figure 8a includes all the GRBs in the Gold/Silver/Aluminum samples, with $\theta_j = 5^\circ$ assumed if the jet angle is not measured. Figure 8b presents those GRBs with jet measurements only. Essentially the same conclusion is reached.

A very interesting question is whether there are noticeable differences between the magnetar and non-magnetar samples. One potential discriminator would be the total energetics of the GRBs. While the magnetar model predicts a maximum value of the total energy (Eq.(1)), the black hole model is not subject to such a limit. In Fig.9 we make some comparisons. The first three panels compare the histograms of the isotropic energies ($E_{\gamma,\text{iso}}$, $E_{K,\text{iso}}$, and $E_{\gamma,\text{iso}} + E_{K,\text{iso}}$) of the magnetar and non-magnetar samples. For the magnetar sample, we in one

⁶ Strictly speaking, these magnetar parameters are the ones after prompt emission is over, since only L_X and L_K are used to derive them. The GRB prompt emission presumably also consumed spin energy and magnetic energy of the magnetar, so the true initial spin period can be somewhat smaller than P_0 , and the true initial (effective) dipole magnetic field at the pole can be somewhat larger than B_p .

case includes the most secure (Gold + Silver) sample only (blue hatched), and in another case includes all magnetar candidates (Gold + Silver + Aluminum) (red solid). The non-magnetar sample is marked in grey. The best Gaussian fits to the three samples are presented as blue, red, and black dotted curves, respectively. The center values of all the fits are presented in Table 3. It is found that without jet correction, the isotropic values of the magnetar and non-magnetar samples are not significantly different.

Next, we introduce beaming correction, and replot the histograms of the jet-corrected energies of the magnetar and non-magnetar samples. The results are presented in the later three panels in Fig.9. One can see a clear distinction between the robust magnetar sample (Gold + Silver) and the non-magnetar sample. For the total energy ($E_\gamma + E_K$), while the former peaks around 50.62 erg, the latter peaks around 51.81 erg. More interestingly, all the Gold+Silver magnetar sample GRBs have a total energy smaller than the limit set by the spin energy (Eq.(1)), while for some non-magnetar sample GRBs, this upper limit is exceeded. The results are generally consistent with the hypothesis that two types of GRB central engines can both power GRBs.

In Fig.10a and Fig.10b, we compare $E_{\gamma,\text{iso}}$ and $E_{K,\text{iso}}$ for the magnetar and non-magnetar samples. The kinetic energy of the blastwave $E_{K,\text{iso}}$ is evaluated at t_b for Fig.10a, and at t_{dec} for Fig.10b (similar to Zhang et al. 2007a). It is interesting to see that at t_{dec} , the magnetar central engine tends to power more efficient GRBs (due to the initial small E_K value) than the black hole central engine. It is interesting to see after the energy injection phase (at t_b), the γ -ray efficiencies of magnetar and non-magnetar samples are no longer significantly different. The same conclusion is also manifested in Fig.11a and 11b, where we plot the histograms of η_γ for different samples.

If one accepts that millisecond magnetars are powering some GRBs, it would be interesting to constrain the internal energy dissipation efficiency η_X (Eq.(24)) from the data. In both Fig.7a and Fig.7b, it is found that the Gold sample GRBs have a relatively large L_b value. This is generally consistent with the expectation that a larger η_X would give rise to an internal plateau (Zhang 2014). In Fig.10c, we compare $L_{K,\text{iso}}$ and $L_{X,\text{iso}}$. It indeed shows that the Gold sample GRBs have a much higher η_X than other GRBs. On the other hand, it is curious to ask why there is a gap in this phase space. It appears that some magnetars are particularly efficient to dissipate the magnetar wind energy, while most magnetars are not. Plotting the histograms of η_X (Fig.11c), it looks indeed like a bimodal distribution of η_X , even though this second high η_X component is not significant enough. In Fig.12, we present the scatter plots of η_X against other parameters, including $\eta_\gamma(t_b)$, $E_{\gamma,\text{iso}}$, $E_{K,\text{iso}}$, and E_{rot} . In all cases, the Gold sample (the ones with very high η_X) tend to stick out and emerge as a separate population.

5. CONCLUSIONS AND DISCUSSION

In order to address whether (at least) some GRBs might have a magnetar central engine, we have systematically analysed the X-ray data of all the *Swift* GRBs (~ 750) detected before August 2013. By applying some criteria to judge how likely a GRB might harbor a mil-

lisecond magnetar central engine, we characterized long GRBs into several samples: Gold, Silver, and Aluminum magnetar samples, as well as the non-magnetar samples. For comparison, we also independently processed the data of short GRBs that might have a magnetar central engine (Rowlinson et al. 2010, 2013). By deriving the basic magnetar parameters P_0 and B_p from the data, we are able to reach two interesting conclusions.

First, it seems that at least for the Gold and Silver sample GRBs, the derived properties seem to be consistent with the expectations of the magnetar central engine model. The consistency includes the following: 1. After beaming correction, the derived P_0 and B_p seem to fall into the reasonable range expected in the magnetar central engine model; 2. The $L_b - t_b$ anti-correlation seems to be consistent with the hypothesis that there is a quasi-universal energy budget defined by the spin energy of the magnetars (Eq.(1)); 3. The sum of E_γ and E_K is generally smaller than E_{rot} , the total energy budget of a magnetar; 4. Most importantly, it seems that the magnetar and non-magnetar samples are different. The robust magnetar sample (Gold + Silver) GRBs all have a beaming-corrected energy smaller than the maximum energy allowed by a magnetar, i.e. $E_{\text{rot,max}} \sim 2 \times 10^{52}$ erg. The non-magnetar sample, on the other hand, can exceed this limit. The two samples have two distinct distributions in E_γ , E_K , and $(E_\gamma + E_K)$, suggesting that they may be powered by different central engines.

Second, both long and short GRBs can be powered by a millisecond magnetar central engine. The characteristic magnetar signature, an internal plateau, is found in both long and short GRBs, suggesting that different progenitors (both massive star core collapses and compact star mergers) can produce a millisecond, probably supra-massive magnetar as the central engine. The data is consistent that a long GRB magnetar wind is collimated, while a short GRB magnetar wind is essentially isotropic. All these have profound implications in several related fields in high-energy, transient astronomy. For example, if the recently discovered fast radio bursts (FRBs, Lorimer et al. 2007; Thornton et al. 2013) are indeed produced when a supra-massive neutron star collapses into a black hole (Falcke & Rezzolla 2014; Zhang 2014), our analysis suggests that such supra-massive neutron stars very likely do exist in GRBs, and that the FRB/GRB association suggested by Zhang (2014) should be quite common, probably up to near half of the entire GRB population. This is higher than the rate of plausible detections made by Bannister et al. (2012), but that low detection rate (2 out of 9 GRBs, Bannister et al. 2012) may be due to the sensitivity limit of the Parkes 12 m telescope they have used. A rapid-slewing larger radio telescope would be able to detect more FRB/GRB associations, which would open a new window to study cosmology (Deng & Zhang 2014) and conduct cosmography (Gao et al. 2014). For another example, the conclusion that short GRBs can be powered by a millisecond magnetar with a near isotropic magnetar wind would give rise to relatively bright, early electromagnetic counterparts of gravitational wave bursts due to NS-NS mergers (Zhang 2013; Gao et al. 2013; Yu et al. 2013; Metzger & Piro 2013; Fan et al. 2013), which gives promising prospects of detecting electromagnetic counterparts of gravitational wave signals in the Advanced LIGO/Virgo

era.

Our analysis also poses some curious questions. One is regarding the magnetar dissipation efficiency η_X . The results seem to suggest that some magnetars are efficient in dissipating their magnetar wind energy to X-ray radiation, while most others are not. A straightforward inference would be that there might be a dichotomy within the magnetar central engines. A more plausible scenario would be that some (or probably) most normal plateaus (those followed by normal decays) could be also dominated by internal dissipation emission (e.g. Ghisellini et al. 2007; Kumar et al. 2008a,b). They are not identified as internal plateaus because their post-break decay is not steep enough. Physically they may be stable magnetars or supra-massive magnetars with a much later collapsing time, so that the collapsing signature (very steep decay) is not detected. If so, the η_X distribution may be more spread out, without a clear bimodal distribution. This possibility is worth exploring in the future.

Another mystery is regarding collimation of magnetar wind in short GRBs. Our analysis suggests that at late times the magnetar wind is essentially isotropic. On the other hand, during the prompt emission phase, at least some short GRBs show evidence of collimation (e.g. Burrows et al. 2006; Soderberg et al. 2006; Berger 2013 for a review). There is no well studied short GRB prompt

emission model within the magnetar central engine scenario. Suggested scenarios invoke an early brief accretion phase (Metzger et al. 2008), an early brief differential rotation phase (Fan et al. 2013), or an early brief phase-transition phase (e.g. Cheng & Dai 1996; Chen & Labun 2013). The short GRB could be collimated by the torus within the accretion scenario (Bucciantini et al. 2012).

Upon finishing this paper, we were drawn attention to Yi et al. (2014), who performed an independent analysis on a sub-sample of GRB magnetar candidates (essentially our Gold sample). They assumed that the long GRB magnetar winds are isotropic and used the data to constrain magnetar wind dissipation efficiencies. Through a comparison with X-ray emission efficiency of spin-down powered pulsars, they offer support to the millisecond magnetar central engine model from a different point of view.

We acknowledge the use of the public data from the Swift data archive and the UK Swift Science Data Center. We thank an anonymous referee for helpful comments, He Gao and En-Wei Liang for helpful discussion, and Zi-Gao Dai, Xue-Feng Wu, and Shuang-Xi Yi for sharing their paper with us and related discussion. This work is supported by the NASA ADAP program under grant NNX10AD48G.

REFERENCES

- Antonelli, L. A., Maund, J. R., Palazzi, E., et al. 2010, GRB Coordinates Network, 10620, 1
- Band, D., Matteson, J., Ford, L., et al. 1993, ApJ, 413, 281
- Bannister, K. W., Murphy, T., Gaensler, B. M., & Reynolds, J. E. 2012, ApJ, 757, 38
- Berger, E. 2013, ARA&A, in press, arXiv:1311.2603
- Bernardini, M. G., Campana, S., Ghisellini, G., et al. 2013, ApJ, 775, 67
- Blandford, R. D., & Znajek, R. L. 1977, MNRAS, 179, 433
- Bloom, J. S., Frail, D. A., & Sari, R. 2001, AJ, 121, 2879
- Bucciantini, N., Quataert, E., Arons, J., Metzger, B. D., Thompson, T. A. 2008, MNRAS, 383, L25
- Bucciantini, N., Metzger, B. D., Thompson, T. A., & Quataert, E. 2012, MNRAS, 419, 1537
- Burrows, D. N., Romano, P., Falcone, A., et al. 2005, Science, 309, 1833
- Burrows, D. N., Grupe, D., Capalbi, M., et al. 2006, ApJ, 653, 468
- Cenko, S. B., Perley, D. A., Jankkarinen, V., et al. 2009, GRB Coordinates Network, 9518, 1
- Chen, P., & Labun, L. 2013, Phys. Rev. D, 88, 083006
- Chen, W.-X., & Beloborodov, A. M. 2007, ApJ, 657, 383
- Cheng, K. S., & Dai, Z. G. 1996, Physical Review Letters, 77, 1210
- Cucchiara, A., & Levan, A. J. 2011, GRB Coordinates Network, 12761, 1
- D’Avanzo, P., D’Elia, V., & Covino, S. 2008, GRB Coordinates Network, 8350, 1
- Dai, Z. G. 2004, ApJ, 606, 1000
- Dai, Z. G., & Lu, T. 1998a, A&A, 333, L87
- Dai, Z. G., & Lu, T. 1998b, Physical Review Letters, 81, 4301
- Dai, Z. G., Wang, X. Y., Wu, X. F., & Zhang, B. 2006, Science, 311, 1127
- Dainotti, M. G., Willingale, R., Capozziello, S., Fabrizio Cardone, V., & Ostrowski, M. 2010, ApJ, 722, L215
- Dall’Osso, S., Stratta, G., Guetta, D., et al. 2011, A&A, 526, A121
- Deng, W., & Zhang, B. 2014, ApJL, in press, arXiv:1401.0059
- Eichler, D., Livio, M., Piran, T., & Schramm, D. N. 1989, Nature, 340, 126
- Evans, P. A., Beardmore, A. P., Page, K. L., et al. 2009, MNRAS, 397, 1177
- Falcke, H., & Rezzolla, L. 2014, A&A, in press, arXiv:1307.1409
- Fan, Y.-Z., & Xu, D. 2006, MNRAS, 372, L19
- Fan, Y.-Z., Yu, Y.-W., Xu, D. et al. 2013, ApJ, 779, L25
- Fan, Y.-Z., Zhang, B.-B., Xu, D., Liang, E.-W., & Zhang, B. 2011, ApJ, 726, 32
- Fishman, G. J., & Meegan, C. A. 1995, ARA&A, 33, 415
- Fong, W., Berger, E., Metzger, B. D., et al. 2014, ApJ, 780, 118
- Frail, D. A., Kulkarni, S. R., Sari, R., et al. 2001, ApJ, 562, L55
- Freiburghaus, C., Rosswog, S., & Thielemann, F.-K. 1999, ApJ, 525, L121
- Fynbo, J. P. U., Tanvir, N. R., D’Elia, V., et al. 2012, GRB Coordinates Network, 14120, 1
- Gao, H., Ding, X., Wu, X.-F., Zhang, B., & Dai, Z.-G. 2013a, ApJ, 771, 86
- Gao, H., Lei W.-H., Zou Y.-C., Wu X.-F., Zhang B., 2013b, NewAR, 57, 141
- Gao, H., Li, Z., & Zhang, B. 2014, ApJL, submitted
- Gao, W.-H., & Fan, Y.-Z. 2006, ChJAA, 6, 513
- Ghisellini, G., Ghirlanda, G., Nava, L., Firmani, C. 2007, ApJ, 658, L75
- Giacomazzo, B., & Perna, R. 2013, ApJ, 771, L26
- Gompertz, B. P., O’Brien, P. T., Wynn, G. A., & Rowlinson, A. 2013, MNRAS, 431, 1745
- Gompertz, B. P., O’Brien, P. T., & Wynn, G. A. 2014, MNRAS, in press (arXiv:1311.1505)
- Grupe, D. et al. 2007, ApJ, 662, 443
- Hotokozaka, K., Kiuchi, K., Kyutoku, K., et al. 2013, Phys. Rev. D, 88, 044026
- Kluźniak, W., & Ruderman, M. 1998, ApJ, 505, L113
- Kumar, P., Narayan, R., Johnson, J. L. 2008a, Science, 321, 376
- Kumar, P., Narayan, R., Johnson, J. L. 2008b, MNRAS, 388, 1729
- Kumar, P., & Panaitescu, A. 2000, ApJ, 541, L9
- Kumar, P., & Zhang, B. 2014, Phys. Rep., submitted
- Landsman, W., de Pasquale, M., Kuin, P., et al. 2008, GRB Coordinates Network, 8601, 1
- Lattimer, J. M., & Prakash, M. 2004, Science, 304, 536
- Lattimer, J. M., Prakash, M., Masak, D., Yahil, A. 1990, ApJ, 355, 241
- Lee, H. K., Wijers, R. A. M. J., & Brown, G. E. 2000, Phys. Rep., 325, 83
- Lei, W. H., Wang, D. X., Zhang, L., et al. 2009, ApJ, 700, 1970
- Lei, W.-H., Zhang, B., & Liang, E.-W. 2013, ApJ, 765, 125

- Levan, A. J., Fynbo, J. P. U., Hjorth, J., et al. 2009, GRB Coordinates Network, 9958, 1
- Levan, A. J., Starling, R., Tanvir, N. R., et al. 2012, GRB Coordinates Network, 13920, 1
- Li, L.-X. 2000, *Phys. Rev. D*, 61, 084016
- Liang, E.-W., Lü, H.-J., Hou, S.-J., Zhang, B.-B., & Zhang, B. 2009, *ApJ*, 707, 328
- Liang, E.-W., Racusin, J. L., Zhang, B., Zhang, B.-B., & Burrows, D. N. 2008, *ApJ*, 675, 528
- Liang, E.-W., Yi, S.-X., Zhang, J., et al. 2010, *ApJ*, 725, 2209
- Liang, E.-W., Zhang, B.-B., & Zhang, B. 2007, *ApJ*, 670, 565
- Lithwick, Y., & Sari, R. 2001, *ApJ*, 555, 540
- Lloyd-Ronning, N. M., & Zhang, B. 2004, *ApJ*, 613, 477
- Lorimer, D. R., Bailes, M., McLaughlin, M. A., Narkevic, D. J., & Crawford, F. 2007, *Science*, 318, 777
- Lu, R.-J., Wei, J.-J., Qin, S.-F., & Liang, E.-W. 2012, *ApJ*, 745, 168
- Lü, H.-J., Zhang, B., Liang, E.-W., Zhang, B.-B., & Sakamoto, T. 2012, *arXiv:1211.1117*
- Lyons, N., O'Brien, P. T., Zhang, B., et al. 2010, *MNRAS*, 402, 705
- MacFadyen, A. I., & Woosley, S. E. 1999, *ApJ*, 524, 262
- Markwardt, C. B. 2009, *Astronomical Data Analysis Software and Systems XVIII*, 411, 251
- Mészáros, P. 2006, *Reports on Progress in Physics*, 69, 2259
- Metzger, B. D., Giannios, D., Thompson, T. A., Bucciantini, N., & Quataert, E. 2011, *MNRAS*, 413, 2031
- Metzger, B. D., Quataert, E., & Thompson, T. A. 2008, *MNRAS*, 385, 1455
- Metzger, B. D., & Piro, A. L. 2013, *arXiv:1311.1519*
- More, J. 1977, in *Numerical Analysis*, vol. 630, 105 (ed. G. A. Watson, Springer-Verlag: Berlin)
- Mundell, C. G. et al. 2007, *ApJ*, 660, 489
- Narayan, R., Paczynski, B., & Piran, T. 1992, *ApJ*, 395, L83
- Narayan, R., Piran, T., & Kumar, P. 2001, *ApJ*, 557, 949
- Nemmen, R. S., Georganopoulos, M., Guiriec, S., et al. 2012, *Science*, 338, 1445
- Nousek, J. A., Kouveliotou, C., Grupe, D., et al. 2006, *ApJ*, 642, 389
- O'Brien, P. T., Willingale, R., Osborne, J., et al. 2006, *ApJ*, 647, 1213
- Paczynski, B. 1986, *ApJ*, 308, L43
- Paczynski, B., 1991, *AcA*, 41, 257
- Panaitescu, A., & Kumar, P. 2002, *ApJ*, 571, 779
- Popham, R., Woosley, S. E., & Fryer, C. 1999, *ApJ*, 518, 356
- Racusin, J. L., Liang, E. W., Burrows, D. N., et al. 2009, *ApJ*, 698, 43
- Rees, M. J., & Meszaros, P. 1998, *ApJ*, 496, L1
- Rezzolla, L., Baiotti, L., Giacomazzo, B., Link, D., & Font, J. A. 2010, *Classical and Quantum Gravity*, 27, 114105
- Rowlinson, A., O'Brien, P. T., Metzger, B. D., Tanvir, N. R., & Levan, A. J. 2013, *MNRAS*, 430, 1061
- Rowlinson, A., O'Brien, P. T., Tanvir, N. R., et al. 2010, *MNRAS*, 409, 531
- Ruffert, M., Janka, H.-T., Takahashi, K., & Schaefer, G. 1997, *A&A*, 319, 122
- Sakamoto, T., Barthelmy, S. D., Barbier, L., et al. 2008, *ApJS*, 175, 179
- Sakamoto, T., Barthelmy, S. D., Baumgartner, W. H., et al. 2011, *ApJS*, 195, 2
- Sakamoto, T., Sato, G., Barbier, L., et al. 2009, *ApJ*, 693, 922
- Salvaterra, R., Campana, S., Vergani, S. D., et al. 2012, *ApJ*, 749, 68
- Sari, R., & Mészáros, P. 2000, *ApJ*, 535, L33
- Schady, P. et al. 2007, *MNRAS*, 380, 1041
- Schulze, S., Levan, A. J., Malesani, D., et al. 2012, GRB Coordinates Network, 13257, 1
- Soderberg, A. M., Berger, E., Kasliwal, M., et al. 2006, *ApJ*, 650, 261
- Tanvir, N. R., Fox, D. B., Levan, A. J., et al. 2009, *Nature*, 461, 1254
- Tanvir, N. R., Fynbo, J. P. U., Melandri, A., et al. 2012, GRB Coordinates Network, 13890, 1
- Tanvir, N. R., Levan, A. J., & Matulonis, T. 2012, GRB Coordinates Network, 14009, 1
- Thoenne, C. C., de Ugarte Postigo, A., Vreeswijk, P., et al. 2010, GRB Coordinates Network, 10971, 1
- Thompson, C. 1994, *MNRAS*, 270, 480
- Thornton, D., Stappers, B., Bailes, M., et al. 2013, *Science*, 341, 53
- Troja, E., Cusumano, G., O'Brien, P. T., et al. 2007, *ApJ*, 665, 599
- Uhm, Z. L., Zhang, B., Hascoët, R., et al. 2012, *ApJ*, 761, 147
- Usov, V. V. 1992, *Nature*, 357, 472
- Virgili, F. J., Qin, Y., Zhang, B., & Liang, E. 2012, *MNRAS*, 424, 2821
- Vreeswijk, P. M., Fynbo, J. P. U., Malesani, D., Hjorth, J., & de Ugarte Postigo, A. 2008, GRB Coordinates Network, 8191, 1
- Wheeler, J. C., Yi, I., Höflich, P., & Wang, L. 2000, *ApJ*, 537, 810
- Wiersema, K., Flores, H., D'Elia, V., et al. 2011, GRB Coordinates Network, 12431, 1
- Wiersema, K., Tanvir, N. R., Cucchiara, A., Levan, A. J., & Fox, D. 2009, GRB Coordinates Network, 10263, 1
- Woosley, S. E. 1993, *ApJ*, 405, 273
- Xu, M., & Huang, Y. F. 2012, *A&A*, 538, A134
- Yi, S. X., Dai, Z. G., Wu, X. F. & Wang, F. Y. 2014, *arXiv:1401.1601*
- Yost, S. A., Harrison, F. A., Sari, R., & Frail, D. A. 2003, *ApJ*, 597, 459
- Yu, Y. W., & Dai, Z. G. 2007, *A&A*, 470, 119
- Yu, Y.-W., Cheng, K. S., & Cao, X.-F. 2010, *ApJ*, 715, 477
- Yu, Y.-W., Zhang, B., & Gao, H. 2013, *ApJ*, 776, L40
- Yuan, F., & Zhang, B. 2012, *ApJ*, 757, 56
- Zhang, B. 2011, *Comptes Rendus Physique*, 12, 206
- Zhang, B. 2013, *ApJ*, 763, L22
- Zhang, B. 2014, *ApJ*, 780, L21
- Zhang, B., Fan, Y. Z., Dyks, J., et al. 2006, *ApJ*, 642, 354
- Zhang, B., Liang, E., Page, K. L., et al. 2007a, *ApJ*, 655, 989
- Zhang, B., & Mészáros, P. 2001, *ApJ*, 552, L35
- Zhang, B., & Mészáros, P. 2004, *International Journal of Modern Physics A*, 19, 2385
- Zhang, B., & Pe'er, A. 2009, *ApJ*, 700, L65
- Zhang, B., Zhang, B.-B., Liang, E.-W., et al. 2007b, *ApJ*, 655, L25
- Zhang, B.-B., Liang, E.-W., & Zhang, B. 2007c, *ApJ*, 666, 1002

TABLE 1
THE γ -RAY AND X-RAY OBSERVATIONS AND FITTING RESULTS OF THE “GOLD”, “SILVER”, AND THE SHORT GRB SAMPLES.

GRB	$T_{90}(\text{s})$	$\Gamma_{\gamma}^{\text{a}}$	$S_{\gamma,-7}^{\text{a}}$	$\beta_{\text{x}}^{\text{b}}$	$(t_1, t_2)(\text{ks})^{\text{c}}$	$t_b(\text{ks})^{\text{d}}$	α_1^{e}	α_2^{e}	χ^2/dof	z^{f}
Gold										
060202	198.9	1.71 \pm 0.13	21.3 \pm 1.65	1.11 \pm 0.03	(0.28,1.7)	0.75 \pm 0.08	0.23 \pm 0.03	5.79 \pm 0.16	563/521	—
060413	147.7	1.68 \pm 0.08	35.6 \pm 1.47	1.28 \pm 0.13	(1.2,253.52)	26.43 \pm 1.12	0.18 \pm 0.03	3.42 \pm 0.21	79/71	—
060522	71.1	1.56 \pm 0.15	11.4 \pm 1.11	1.18 \pm 0.17	(0.2,0.9)	0.53 \pm 0.06	0.14 \pm 0.36	3.15 \pm 0.79	12/11	5.11 ⁽¹⁾
060607A	102.2	1.47 \pm 0.08	25.5 \pm 1.12	0.67 \pm 0.06	(1.52,39.52)	12.34 \pm 0.19	0 \pm 0.01	3.4 \pm 0.06	132/139	3.082 ⁽¹⁾
070110	88.4	1.58 \pm 0.12	18 \pm 2	1.12 \pm 0.07	(4.1,28.72)	20.4 \pm 0.44	0.11 \pm 0.05	8.7 \pm 0.8	44/46	2.352 ⁽¹⁾
070616	402.4	1.61 \pm 0.04	192 \pm 3.47	0.26 \pm 0.01	(0.13,2.01)	0.53 \pm 0.04	-0.11 \pm 0.02	5.29 \pm 0.05	224/241	—
090419	450	1.38 \pm 0.16	25 \pm 2	0.30 \pm 0.28	(0.12,1.72)	0.49 \pm 0.07	0.2 \pm 0.2	3.44 \pm 0.23	77/72	—
120213A	49	2.37 \pm 0.09	19 \pm 1	0.95 \pm 0.21	(1.04,12.84)	8.03 \pm 0.97	0.35 \pm 0.06	4.56 \pm 0.24	49/53	—
130102A	77.5	1.39 \pm 0.18	7.2 \pm 0.9	0.80 \pm 0.41	(0.18,10)	0.42 \pm 0.26	0.22 \pm 0.41	5.92 \pm 0.57	12/10	—
Silver										
	(those	with	measured	redshifts	only)					
050401	33.3	1.4 \pm 0.07	82.2 \pm 3.06	0.82 \pm 0.15	(0.13,548)	5.86 \pm 0.78	0.57 \pm 0.02	1.37 \pm 0.06	107/92	2.9 ⁽¹⁾
050505	58.9	1.41 \pm 0.12	24.9 \pm 1.79	1.23 \pm 0.04	(2.88,133)	7.87 \pm 1.57	0.19 \pm 0.15	1.3 \pm 0.06	27/45	4.27 ⁽¹⁾
050803	87.9	1.38 \pm 0.11	21.5 \pm 1.35	1.23 \pm 0.12	(0.32,1330)	15.98 \pm 0.18	0.38 \pm 0.02	1.89 \pm 0.06	95/75	0.422 ⁽¹⁾
060108	14.3	2.03 \pm 0.17	3.69 \pm 0.37	1.21 \pm 0.28	(0.75,368)	14.24 \pm 7.38	0.12 \pm 0.08	1.25 \pm 0.06	7/7	2.03 ⁽¹⁾
060526	298.2	2.01 \pm 0.24	12.6 \pm 1.65	1.16 \pm 0.16	(1.02,314)	10.02 \pm 4.55	0.31 \pm 0.12	1.5 \pm 0.23	34/48	3.21 ⁽¹⁾
060604	95	2.01 \pm 0.42	4.02 \pm 1.06	1.15 \pm 0.17	(1.23,824)	11.37 \pm 6.8	0.19 \pm 0.48	1.17 \pm 0.08	35/41	2.1357 ⁽¹⁾
060605	79.1	1.55 \pm 0.2	6.97 \pm 0.9	1.36 \pm 0.12	(0.15,103)	7.45 \pm 0.52	0.45 \pm 0.03	2.01 \pm 0.05	16/21	3.78 ⁽¹⁾
060614	108.7	2.02 \pm 0.04	204 \pm 3.63	1.18 \pm 0.09	(4.54,1795)	49.84 \pm 3.62	0.18 \pm 0.06	1.9 \pm 0.07	70/54	0.125 ⁽¹⁾
060729	115.3	1.75 \pm 0.14	26.1 \pm 2.11	1.24 \pm 0.03	(0.52,8968)	72.97 \pm 3.02	0.21 \pm 0.01	1.42 \pm 0.02	160/459	0.54 ⁽¹⁾
060906	43.5	2.03 \pm 0.11	22.1 \pm 1.36	1.12 \pm 0.17	(0.42,258)	12.78 \pm 3.29	0.3 \pm 0.04	1.81 \pm 0.1	5/7	3.685 ⁽¹⁾
060908	19.3	1.01 \pm 0.3	28 \pm 1.11	1.40 \pm 0.30	(0.08,14.8)	0.71 \pm 0.17	0.43 \pm 0.09	1.56 \pm 0.06	98/59	1.8836 ⁽¹⁾
061110A	40.7	1.67 \pm 0.12	10.6 \pm 0.76	1.10 \pm 0.32	(3.08,756)	73.17 \pm 5.67	0.19 \pm 0.15	1.16 \pm 0.17	7/5	0.758 ⁽¹⁾
070306	209.5	1.66 \pm 0.1	53.8 \pm 2.86	1.19 \pm 0.08	(0.48,819)	29.69 \pm 1.72	0.12 \pm 0.02	1.87 \pm 0.03	153/132	1.497 ⁽¹⁾
070529	109.2	1.34 \pm 0.16	25.7 \pm 2.45	0.76 \pm 0.24	(0.17,445)	1.65 \pm 0.84	0.64 \pm 0.07	1.36 \pm 0.05	23/19	2.4996 ⁽¹⁾
080605	20	1.11 \pm 0.14	133 \pm 2	0.74 \pm 0.16	(0.09,101)	0.44 \pm 0.05	0.5 \pm 0.05	1.34 \pm 0.02	330/289	1.6398 ⁽¹⁾
080607	79	1.31 \pm 0.04	240 \pm 9	1.13 \pm 0.15	(0.62,401)	1.38 \pm 0.19	0.05 \pm 0.33	1.68 \pm 0.04	103/98	3.036 ⁽¹⁾
080721	16.2	1.11 \pm 0.08	120 \pm 10	0.84 \pm 0.06	(0.11,2011)	3.09 \pm 0.16	0.8 \pm 0.01	1.65 \pm 0.02	54/49	2.602 ⁽¹⁾
080905B	128	1.78 \pm 0.15	18 \pm 2	1.22 \pm 0.10	(0.22,988)	4.03 \pm 1.22	0.25 \pm 0.03	1.46 \pm 0.02	94/98	2.374 ⁽²⁾
081008	185.5	1.69 \pm 0.07	43 \pm 2	0.98 \pm 0.11	(0.71,502)	15.92 \pm 6.58	0.81 \pm 0.03	1.85 \pm 0.08	33/38	1.9685 ⁽³⁾
081203A	294	1.54 \pm 0.06	77 \pm 3	1.04 \pm 0.11	(0.2,506)	11.23 \pm 8.69	1.12 \pm 0.01	2.07 \pm 0.07	191/163	2.1 ⁽⁴⁾
081221	34	1.21 \pm 0.13	181 \pm 3	1.29 \pm 0.10	(0.25,498)	0.6 \pm 0.08	0.3 \pm 0.11	1.32 \pm 0.02	285/312	2.26 ⁽⁵⁾
090423	10.3	0.8 \pm 0.5	5.9 \pm 0.4	0.92 \pm 0.16	(0.39,501)	4.28 \pm 0.76	-0.16 \pm 0.07	1.42 \pm 0.04	27/33	8.2 ⁽⁶⁾
090618	113.2	1.42 \pm 0.09	1050 \pm 10	0.72 \pm 0.05	(0.58,1998)	7.28 \pm 1.43	0.67 \pm 0.02	1.48 \pm 0.03	128/132	0.54 ⁽⁷⁾
090927	2.2	1.8 \pm 0.2	2 \pm 0.3	0.92 \pm 0.23	(2.52,1003)	8.29 \pm 1.32	0.16 \pm 0.11	1.24 \pm 0.09	19/15	1.37 ⁽⁸⁾
091208B	14.9	1.74 \pm 0.11	33 \pm 2	1.04 \pm 0.16	(0.14,969)	1.15 \pm 0.21	0.16 \pm 0.14	1.17 \pm 0.03	79/68	1.063 ⁽⁹⁾
100418A	7	2.16 \pm 0.25	3.4 \pm 0.5	1.27 \pm 0.23	(0.51,2002)	86.82 \pm 22.14	-0.11 \pm 0.05	1.53 \pm 0.06	44/49	0.6235 ⁽¹⁰⁾
111008A	63.5	1.86 \pm 0.09	53 \pm 3	1.07 \pm 0.23	(0.31,987)	7.47 \pm 2.28	0.29 \pm 0.02	1.34 \pm 0.02	143/167	4.9898 ⁽¹¹⁾
111228A	101.2	2.27 \pm 0.06	85 \pm 2	1.12 \pm 0.08	(0.42,2990)	6.53 \pm 2.11	0.22 \pm 0.03	1.23 \pm 0.01	202/187	0.7156 ⁽¹²⁾
120422A	5.35	1.19 \pm 0.24	2.3 \pm 0.4	1.22 \pm 0.23	(0.49,2011)	166.15 \pm 22.33	0.27 \pm 0.04	1.27 \pm 0.14	4/6	0.283 ⁽¹³⁾
121024A	69	1.41 \pm 0.22	11 \pm 1	0.94 \pm 0.14	(2.01,504)	32.98 \pm 8.21	0.8 \pm 0.06	1.71 \pm 0.09	47/52	2.298 ⁽¹⁴⁾
121027A	62.6	1.82 \pm 0.09	20 \pm 1	1.45 \pm 0.11	(40.1,3019)	144.71 \pm 44.87	0.37 \pm 0.07	1.52 \pm 0.05	54/46	1.773 ⁽¹⁵⁾
121128A	23.3	1.32 \pm 0.18	69 \pm 4	1.32 \pm 0.21	(0.21,98.7)	1.58 \pm 0.24	0.52 \pm 0.07	1.68 \pm 0.04	81/78	2.2 ⁽¹⁶⁾
121229A	100	2.43 \pm 0.46	4.6 \pm 1.3	1.10 \pm 0.30	(2.04,205)	56.39 \pm 8.34	0.21 \pm 0.12	1.43 \pm 0.27	3/5	2.707 ⁽¹⁷⁾
SGRBs										
	(those	with	measured	redshifts	only)					
051221A	1.4	1.39 \pm 0.06	11.5 \pm 0.35	1.07 \pm 0.13	(6.02,655)	34.32 \pm 6.78	0.19 \pm 0.08	1.45 \pm 0.05	41/44	0.55 ⁽¹⁸⁾
060801	0.49	1.27 \pm 0.16	0.8 \pm 0.1	0.43 \pm 0.12	(0.08,0.73)	0.06 \pm 0.04	0.67 \pm 0.12	4.81 \pm 0.62	22/18	1.131 ⁽¹⁸⁾
061201	0.6	0.81 \pm 0.15	3.24 \pm 0.27	1.2 \pm 0.22	(0.11,30.9)	1.21 \pm 0.26	0.52 \pm 0.06	1.87 \pm 0.07	16/18	0.111 ⁽¹⁸⁾
070809	1.3	1.69 \pm 0.22	1.0 \pm 0.1	0.37 \pm 0.21	(0.53,67.4)	12.86 \pm 6.52	-0.01 \pm 0.09	1.14 \pm 0.13	33/26	0.219 ⁽¹⁸⁾
090426	1.2	1.93 \pm 0.22	1.8 \pm 0.3	1.04 \pm 0.15	(0.13,17.6)	0.31 \pm 0.18	-0.18 \pm 0.16	1.02 \pm 0.04	25/19	2.6 ⁽¹⁸⁾
090510	0.3	0.98 \pm 0.21	3.4 \pm 0.4	0.75 \pm 0.12	(0.11,20.7)	0.28 \pm 0.04	0.62 \pm 0.03	2.17 \pm 0.05	76/68	0.903 ⁽¹⁸⁾
100724A	1.4	1.92 \pm 0.21	1.6 \pm 0.2	0.94 \pm 0.23	(0.38,0.89)	0.52 \pm 0.16	0.21 \pm 0.12	1.84 \pm 0.51	45/33	1.288 ⁽¹⁹⁾
101219A	0.6	0.63 \pm 0.09	4.6 \pm 0.3	0.53 \pm 0.26	(0.05,0.27)	0.23 \pm 0.15	0.21 \pm 0.24	6.82 \pm 0.96	38/29	0.718 ⁽¹⁸⁾
130603B	0.18	1.83 \pm 0.12	19.2 \pm 1.2	1.18 \pm 0.18	(0.07,48.1)	3.01 \pm 0.67	0.38 \pm 0.02	1.64 \pm 0.04	111/98	0.356 ⁽²⁰⁾

REFERENCES. — 1: Evans et al.(2009); 2: Vreeswijk et al.(2008); 3: D’Avanzo et al.(2008); 4: Landsman et al.(2008); 5: Salvaterra et al.(2012); 6: Tanvir et al.(2009); 7: Cenko et al.(2009); 8: Levan et al.(2009); 9: Wiersema et al.(2009); 10: Antonelli et al.(2010); 11: Wiersema et al.(2011); 12: Cucchiara et al.(2011); 13: Schulze et al.(2012); 14: Tanvir et al.(2012); 15: Levan et al.(2012); 16: Tanvir et al.(2012); 17: Fynbo et al.(2012); 18: Rowlinson et al.(2013); 19: Thoene et al.(2010); 20: Fong et al.(2014).

^a The photon index and gamma-ray fluence in the BAT band (15–150keV, in units of 10^{-7} erg cm $^{-2}$).

^b The spectral index of the absorbed power-law model for the plateau or the normal segments.

^c Time interval (from t_1 to t_2) of our XRT light curve fitting; times in units of kilo seconds.

^d The break time of the lightcurves from our fitting.

^e α_1 and α_2 are the decay slopes before and after the break time.

^f The References of redshift measurements.

TABLE 2
THE PROPERTIES OF GRBs WITH KNOWN REDSHIFTS IN OUR “GOLD”, “SILVER”, AND SHORT GRB SAMPLES.

GRB	θ_j^a	$E_{\gamma, \text{iso}, 52}^b$	$L_{b, 49}^c$	τ_3^c	$B_{p, 15}^d$	$P_{0, -3}^d$	$B_{p, \theta, 15}^e$	$P_{0, \theta, -3}^e$	$E_{\text{rot}, 50}^f$
Gold									
060522	5	0.71 ± 0.71	1.38 ± 0.22	0.06 ± 0.01	2.34 ± 0.71	1.19 ± 0.59	37.93 ± 11.42	19.28 ± 9.51	0.54 ± 0.29
060607A	5	9.08 ± 7.11	0.58 ± 0.07	0.13 ± 0.02	0.18 ± 0.04	0.44 ± 0.10	2.91 ± 0.67	7.15 ± 1.58	3.91 ± 1.29
070110	5	3.09 ± 2.51	0.07 ± 0.03	3.68 ± 0.06	0.23 ± 0.11	0.74 ± 0.36	3.79 ± 1.78	11.97 ± 5.84	1.39 ± 0.76
Silver									
050401	5	32^{+26}_{-7}	0.47 ± 0.01	1.51 ± 0.21	0.09 ± 0.02	0.15 ± 0.02	1.44 ± 0.32	2.43 ± 0.34	34.20 ± 8.11
050505	1.67 ± 0.35	16^{+13}_{-3}	0.41 ± 0.01	1.49 ± 0.30	0.07 ± 0.02	0.13 ± 0.03	3.21 ± 1.20	6.28 ± 1.45	5.12 ± 1.78
050803	5	$0.24^{+0.24}_{-0.08}$	$(8.92 \pm 0.31)\text{e-}4$	11.24 ± 0.13	0.07 ± 0.01	0.21 ± 0.01	1.22 ± 0.04	3.39 ± 0.08	17.37 ± 7.88
060108	5	$0.59^{+0.84}_{-0.08}$	$(5.96 \pm 0.48)\text{e-}3$	4.70 ± 2.44	0.21 ± 0.36	0.53 ± 0.50	3.28 ± 0.58	8.65 ± 2.43	2.68 ± 1.79
060526	3.61 ± 0.57	$5.2^{+5.6}_{-0.4}$	$(3.91 \pm 0.27)\text{e-}2$	2.38 ± 1.08	0.10 ± 0.09	0.21 ± 0.18	2.14 ± 1.59	4.74 ± 1.98	8.93 ± 2.69
060604	5	$0.5^{+0.12}_{-0.1}$	$(1.15 \pm 0.05)\text{e-}2$	3.63 ± 2.17	0.21 ± 0.08	0.49 ± 0.36	3.39 ± 1.87	7.98 ± 3.88	3.16 ± 2.45
060605	1.55 ± 0.57	$2.5^{+3.1}_{-0.6}$	0.13 ± 0.01	1.56 ± 0.11	0.03 ± 0.01	0.06 ± 0.01	1.68 ± 0.23	3.19 ± 0.31	19.57 ± 3.35
060614	7.57 ± 2.29	$0.24^{+0.04}_{-0.04}$	$(2.49 \pm 0.08)\text{e-}5$	44.31 ± 3.22	0.06 ± 0.01	0.32 ± 0.03	0.69 ± 0.10	3.42 ± 0.34	17.06 ± 2.92
060729	18 ± 1.61	$0.33^{+0.29}_{-0.06}$	$(1.56 \pm 0.02)\text{e-}3$	47.38 ± 1.96	0.06 ± 0.01	0.33 ± 0.02	0.25 ± 0.02	1.48 ± 0.07	91.23 ± 7.84
060906	1.15 ± 0.12	13^{+12}_{-1}	$(3.08 \pm 0.21)\text{e-}2$	2.73 ± 0.70	0.04 ± 0.02	0.09 ± 0.04	2.55 ± 1.70	6.36 ± 2.78	4.94 ± 2.55
060908	0.46 ± 0.29	7^{+4}_{-1}	0.26 ± 0.07	0.25 ± 0.06	0.57 ± 0.41	0.33 ± 0.17	100.6 ± 73.24	59.08 ± 30.06	0.06 ± 0.03
061110A	5	$0.28^{+0.28}_{-0.06}$	$(3.83 \pm 0.81)\text{e-}5$	41.62 ± 3.23	0.39 ± 0.09	2.32 ± 0.41	6.31 ± 1.43	37.68 ± 6.71	0.14 ± 0.04
070306	3.38 ± 1.72	6^{+5}_{-1}	$(2.06 \pm 0.06)\text{e-}2$	11.89 ± 0.69	0.02 ± 0.01	0.06 ± 0.01	0.36 ± 0.04	1.39 ± 0.11	104.2 ± 14.5
070529	5	9^{+9}_{-3}	0.12 ± 0.01	0.47 ± 0.24	0.44 ± 0.17	0.39 ± 0.33	7.06 ± 1.58	6.33 ± 3.63	5.02 ± 3.55
080605	5	21^{+9}_{-4}	1.49 ± 0.16	0.17 ± 0.02	0.47 ± 0.11	0.22 ± 0.03	7.63 ± 1.75	3.52 ± 0.56	16.26 ± 4.22
080607	5	280^{+130}_{-90}	1.36 ± 0.27	0.34 ± 0.05	0.13 ± 0.05	0.11 ± 0.03	2.10 ± 0.77	1.72 ± 0.47	67.85 ± 26.14
080721	5	110^{+110}_{-50}	2.50 ± 0.13	0.86 ± 0.04	0.07 ± 0.01	0.09 ± 0.01	1.18 ± 0.12	1.45 ± 0.10	96.86 ± 13.41
080905B	5	$3.4^{+3.1}_{-0.6}$	0.31 ± 0.01	1.20 ± 0.36	0.11 ± 0.08	0.16 ± 0.07	1.84 ± 1.30	2.58 ± 1.10	30.32 ± 15.55
081008	5	6^{+3}_{-1}	$(1.19 \pm 0.06)\text{e-}2$	5.36 ± 2.22	0.08 ± 0.10	0.22 ± 0.16	1.29 ± 0.63	3.60 ± 1.63	15.45 ± 10.29
081203A	5	17^{+13}_{-4}	$(3.23 \pm 0.11)\text{e-}2$	3.62 ± 2.80	0.06 ± 0.01	0.13 ± 0.07	0.93 ± 0.39	2.17 ± 0.73	42.65 ± 4.11
081221	5	282.29 ± 4.68	1.72 ± 0.20	0.18 ± 0.02	0.38 ± 0.11	0.21 ± 0.04	6.19 ± 1.79	3.35 ± 0.67	18.01 ± 5.61
090423	> 12	8^{+1}_{-1}	0.82 ± 0.04	0.47 ± 0.08	0.19 ± 0.07	0.28 ± 0.07	1.30 ± 0.47	1.88 ± 0.44	59.46 ± 22.42
090618	6.7 ± 1.08	15^{+1}_{-1}	$(1.62 \pm 0.02)\text{e-}2$	4.73 ± 0.93	0.25 ± 0.09	0.48 ± 0.13	3.08 ± 1.09	5.79 ± 1.23	5.98 ± 1.94
090927	5	0.43 ± 0.06	$(5.16 \pm 0.27)\text{e-}3$	55.36 ± 32.68	0.05 ± 0.02	0.36 ± 0.25	0.73 ± 0.21	5.82 ± 0.86	6.01 ± 1.04
091208B	7.3 ± 1.42	4.88 ± 0.30	0.05 ± 0.01	0.56 ± 0.10	0.96 ± 0.60	0.72 ± 0.34	10.71 ± 6.65	8.02 ± 3.77	3.11 ± 1.67
100418A	5	0.14 ± 0.02	$(1.16 \pm 0.11)\text{e-}4$	53.48 ± 13.64	0.05 ± 0.03	0.32 ± 0.13	0.80 ± 0.51	5.23 ± 2.16	7.31 ± 3.65
111008A	5	85.23 ± 4.82	0.72 ± 0.02	1.25 ± 0.38	0.05 ± 0.04	0.11 ± 0.04	0.88 ± 0.59	1.67 ± 0.67	72.35 ± 35.86
111228A	5	5.45 ± 0.13	$(8.48 \pm 0.24)\text{e-}3$	3.81 ± 1.23	0.36 ± 0.25	0.64 ± 0.26	5.78 ± 1.19	10.32 ± 4.22	1.89 ± 0.94
120422A	5	0.13 ± 0.02	$(2.31 \pm 0.26)\text{e-}6$	129.5 ± 17.4	0.42 ± 0.12	3.80 ± 0.75	6.85 ± 1.96	61.66 ± 12.09	0.05 ± 0.02
121024A	5	10.78 ± 0.98	$(6.30 \pm 0.45)\text{e-}3$	10.01 ± 2.49	0.06 ± 0.02	0.26 ± 0.09	1.05 ± 0.58	4.19 ± 1.48	11.38 ± 5.16
121027A	5	6.61 ± 0.33	$(3.38 \pm 0.16)\text{e-}3$	52.19 ± 16.18	0.02 ± 0.01	0.15 ± 0.07	0.29 ± 0.15	2.41 ± 1.09	34.58 ± 18.26
121128A	5	78.91 ± 4.57	0.38 ± 0.06	0.50 ± 0.08	0.21 ± 0.08	0.18 ± 0.05	3.39 ± 1.29	2.98 ± 0.82	22.61 ± 8.72
121229A	5	6.64 ± 1.88	$(1.81 \pm 0.25)\text{e-}3$	15.21 ± 2.25	0.07 ± 0.02	0.34 ± 0.08	1.06 ± 0.36	5.55 ± 1.32	6.52 ± 2.27
SGRBs									
051221A	-	$0.28^{+0.21}_{-0.11}$	24.71 ± 4.97	$(8.8 \pm 0.23)\text{e-}3$	0.57 ± 0.01	2.47 ± 0.16	-	-	22.88 ± 4.41
060801	-	$0.17^{+0.02}_{-0.02}$	0.03 ± 0.02	8.7 ± 4.1	11.21 ± 4.21	1.95 ± 0.34	-	-	52.62 ± 24.26
061201	-	$0.018^{+0.002}_{-0.001}$	1.08 ± 0.23	0.08 ± 0.01	6.01 ± 0.12	4.59 ± 0.05	-	-	9.48 ± 1.88
070809	-	$0.001^{+0.001}_{-0.001}$	12.14 ± 5.33	$(4.5 \pm 2.5)\text{e-}3$	2.06 ± 1.03	5.55 ± 1.25	-	-	6.49 ± 4.31
090426	-	$0.42^{+0.5}_{-0.04}$	0.09 ± 0.05	1.9 ± 1.2	4.79 ± 3.11	1.87 ± 0.53	-	-	57.46 ± 5.44
090510	-	$0.3^{+0.5}_{-0.2}$	0.15 ± 0.02	2.1 ± 0.2	5.05 ± 0.26	1.87 ± 0.05	-	-	57.36 ± 3.02
100724A	-	$0.07^{+0.01}_{-0.01}$	0.23 ± 0.07	0.23 ± 0.03	8.22 ± 0.59	4.14 ± 0.15	-	-	11.67 ± 1.87
101219A	-	$0.48^{+0.03}_{-0.03}$	0.13 ± 0.06	9.7 ± 3.8	2.86 ± 0.81	0.96 ± 0.13	-	-	217.7 ± 71.5
130603B	-	$0.22^{+0.02}_{-0.02}$	2.22 ± 0.49	0.11 ± 0.01	2.16 ± 0.12	2.61 ± 0.07	-	-	29.32 ± 1.63

^a The jet opening angle (in units of degree ($^\circ$)) measured from afterglow observations (Racusin et al. 2009; Lu et al. 2011; Nemmen et al. 2012), or assumed as $\theta_j = 5^\circ$ if no observation is available. SGRBs are assumed to be isotropic.

^b $E_{\gamma, \text{iso}}$ is calculated using fluence and redshift extrapolated into 1-10000 keV (rest frame) with a spectral model and a k-correction, in units of 10^{52} erg.

^c Isotropic luminosity of break time (in units of 10^{49} erg s^{-1}), and the spin-down time (in units of 10^3 s).

^d Dipolar magnetic field strength at the polar cap in units of 10^{15} G, and the initial spin period of the magnetar in units of milliseconds, with an assumption of an isotropic wind.

^e The same as d , but with beaming correction made.

^f The rotational energy (in units of 10^{50} erg) of the magnetar assuming $R_6 = 1$ and $M = 1.4 M_\odot$.

TABLE 3
THE CENTER VALUE OF GAUSSIAN FITTING OF THE
DISTRIBUTIONS.

	Gold+Silver	Gold+Silver+Aluminum	Non-magnetar
$E_{\gamma, \text{iso}}$	(52.87 ± 0.33) erg	(52.89 ± 0.09) erg	(53.20 ± 0.04) erg
$E_{\text{K}, \text{iso}}$	(53.11 ± 0.09) erg	(53.99 ± 0.06) erg	(53.94 ± 0.02) erg
$E_{\text{total}, \text{iso}}$	(53.31 ± 0.05) erg	(54.05 ± 0.05) erg	(54.01 ± 0.05) erg
	Silver	Silver+Aluminum	Non-magnetar
E_{γ}	(48.55 ± 0.11) erg	(49.06 ± 0.13) erg	(50.11 ± 0.12) erg
E_{K}	(50.55 ± 0.17) erg	(51.13 ± 0.12) erg	(51.54 ± 0.18) erg
E_{total}	(50.62 ± 0.07) erg	(51.06 ± 0.09) erg	(51.81 ± 0.11) erg

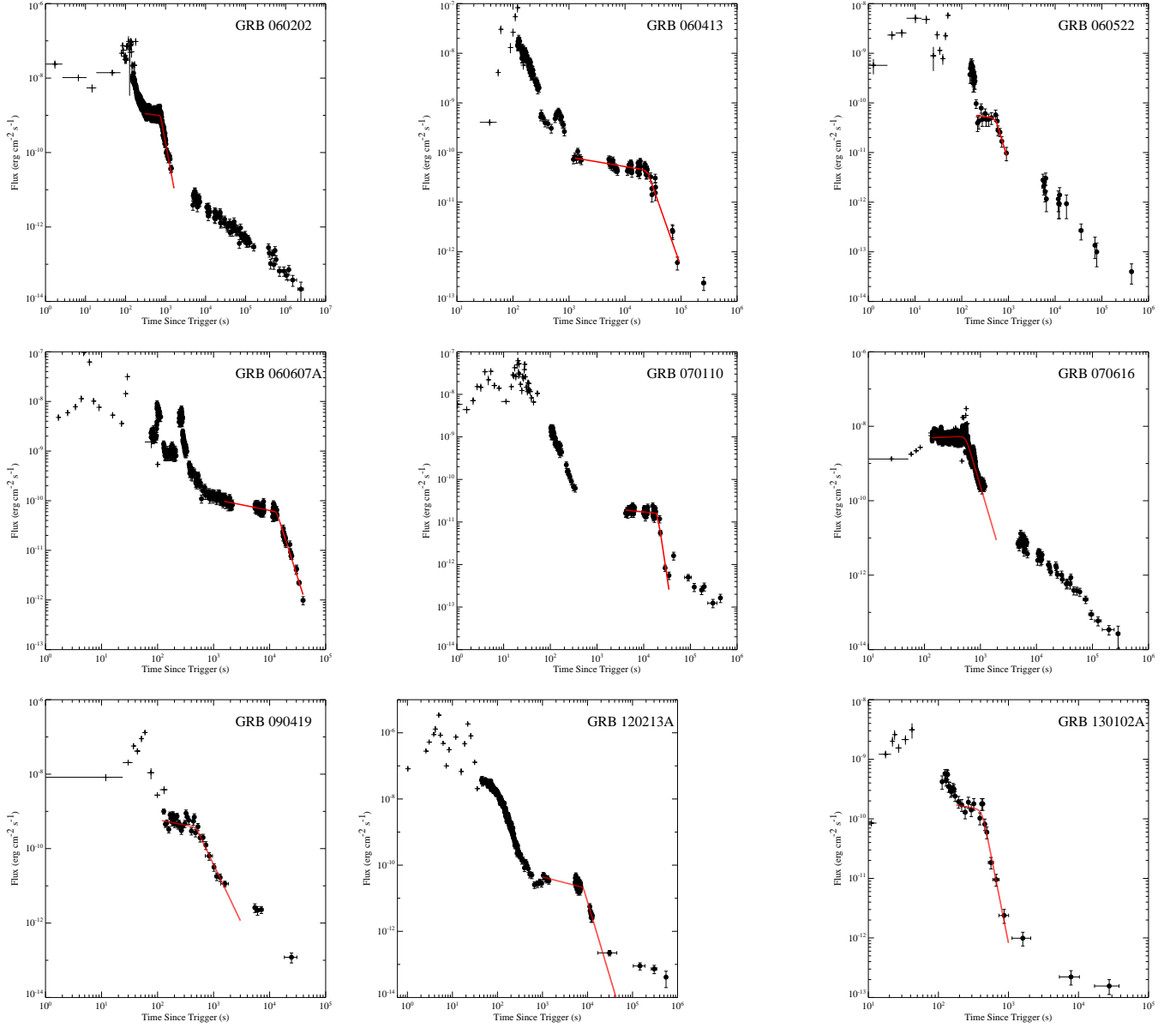


FIG. 1.— The X-ray light curves of the GRBs in our Gold sample. Plus signs are BAT data extrapolated to the XRT band, and points (with error bars) are the XRT data. The red solid curves are the best fits of the smooth broken power law model to the data.

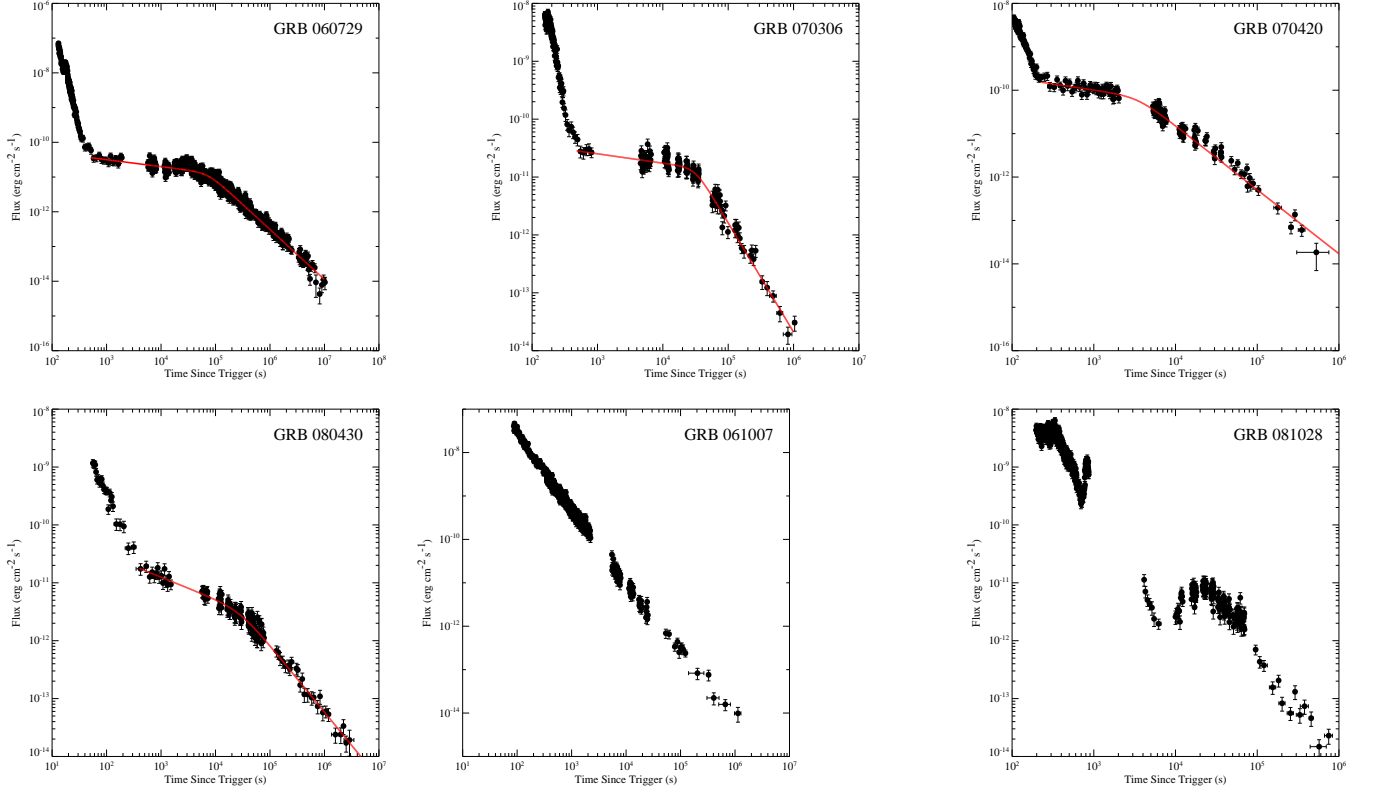


FIG. 2.— Two cases of the X-ray light curves in our Silver (GRB 060729 and 070306), Aluminum (GRB 070420 and 080430), and Non-magnetar (GRB 061007 and 081028) sample. The red solid curves are the best fits of the smooth broken power law model to the data.

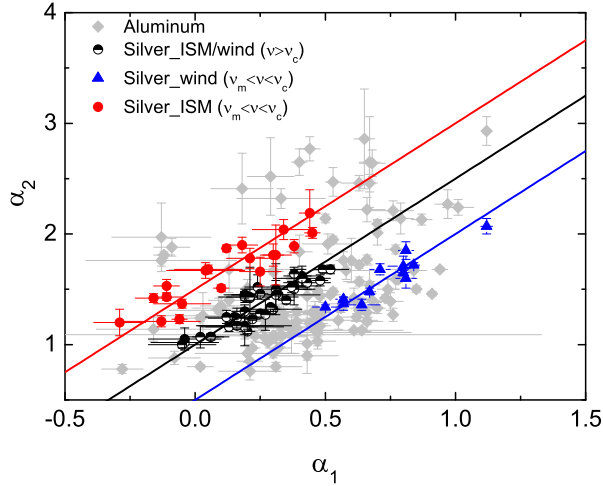


FIG. 3.— The temporal decay indices α_1 vs. α_2 for the “Silver” and “Aluminum” samples. The three solid lines indicate the closure relations of three specific external shock models invoking energy injection with the parameter $q = 0$, as is expected in the millisecond magnetar central engine model. The colored data points belong to the Silver sample, while grey data points belong to the Aluminum sample.

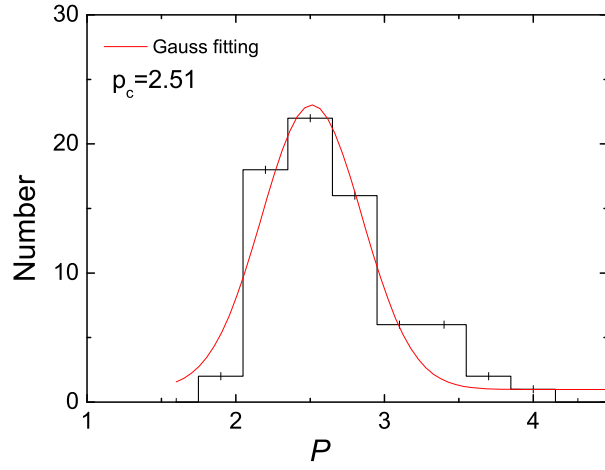


FIG. 4.— The distribution of electron spectral index p derived from the Silver sample. The solid line is the best Gaussian fit with a center value $p_c = 2.51$.

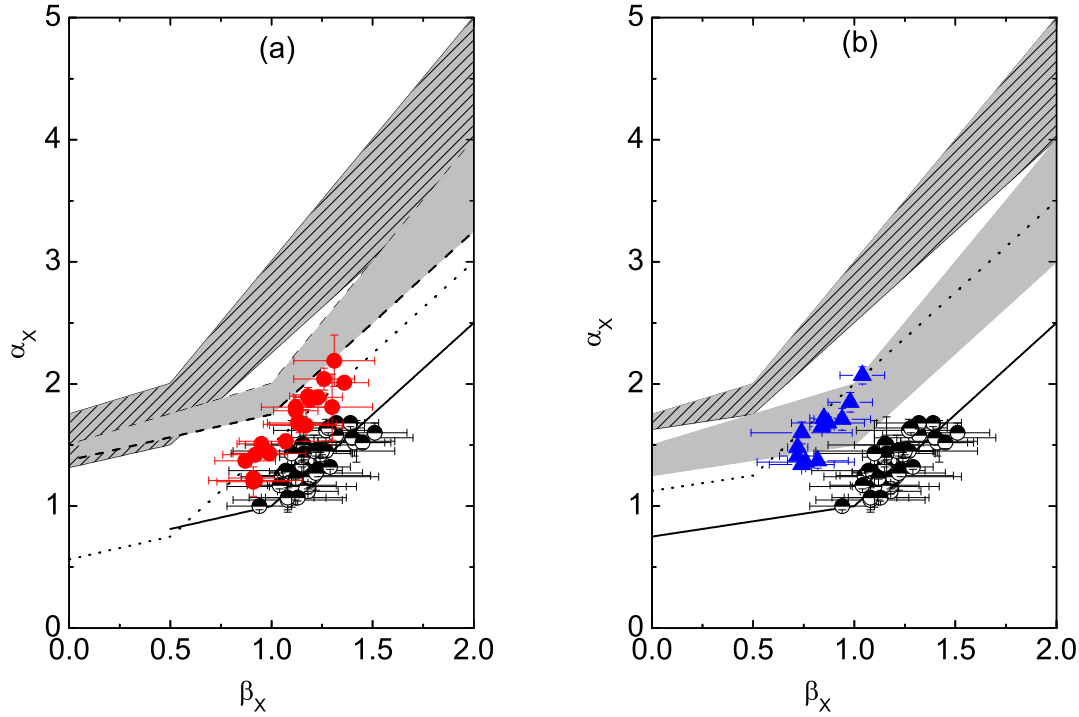


FIG. 5.— The temporal decay index α against spectral index β along with the closure relations of the external shock models for the “Silver” sample. (a) The case of the ISM model: the solid line (pre- jet break) and the shaded region (post jet break) are for the spectral regime I ($\nu_x > \max(\nu_m, \nu_c)$), while the dashed line (pre- jet break) and hatched region (post jet break) are for the spectral regime II ($\nu_m < \nu_x < \nu_c$). Half-solid (black) dots and solid (red) dots are for regime I and II, respectively. (b) The case of the wind medium case. Same conventions, except that triangles (blue) denote the spectral regime II.

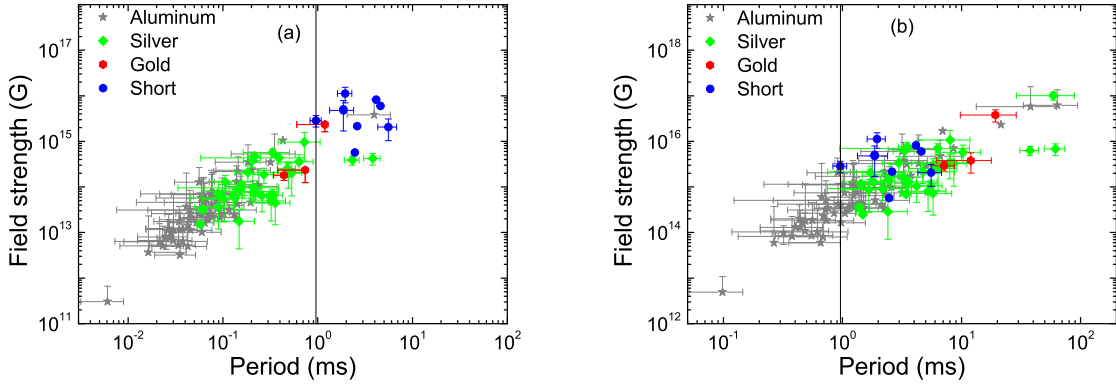


FIG. 6.— The inferred magnetar parameters, initial spin period P_0 vs. surface polar cap magnetic field strength B_p derived for different magnetar samples: Gold (red hexagons), Silver (green diamonds), Aluminum (grey), and short GRBs (blue). (a) The case of isotropic winds; (b) The case with beaming corrections. The vertical solid line is the breakup spin-period for a neutron star (Lattimer & Prakash 2004).

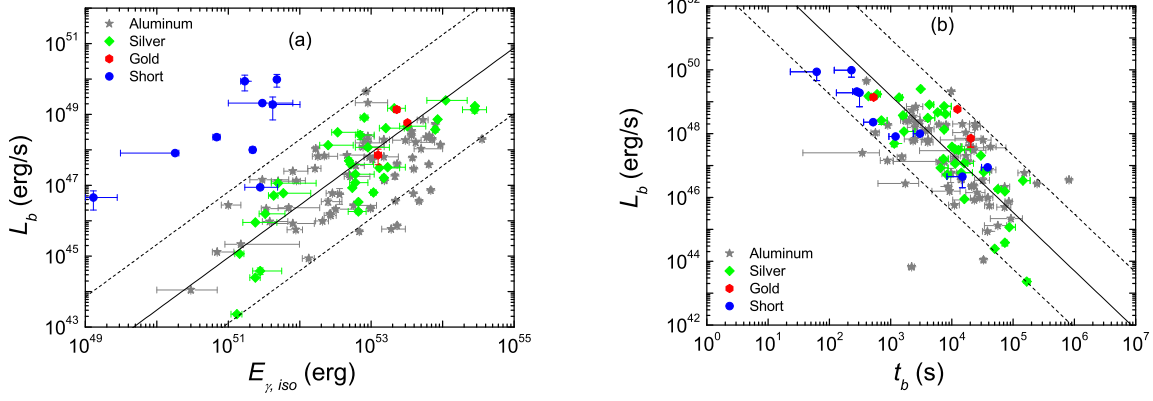


FIG. 7.— The $L_b - E_{\gamma,iso}$ and $L_b - t_b$ correlations for the GRBs in various magnetar samples. The color convention is the same as Fig. 5. The solid line is a power-law fitting to the Gold and Silver sample GRBs, and the two dashed lines denote the 2σ region of the fits.

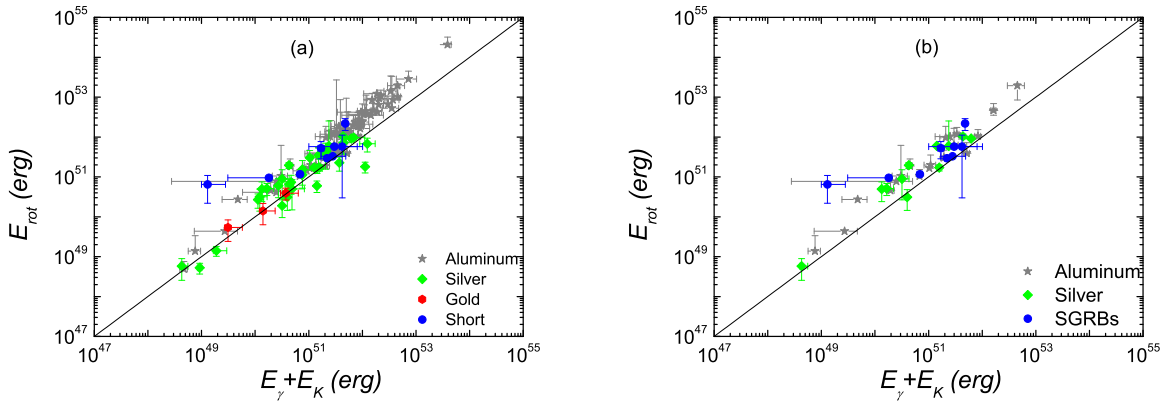


FIG. 8.— A comparison between $(E_{\gamma} + E_K)$ and E_{rot} . The color convention is the same as Fig. 5.

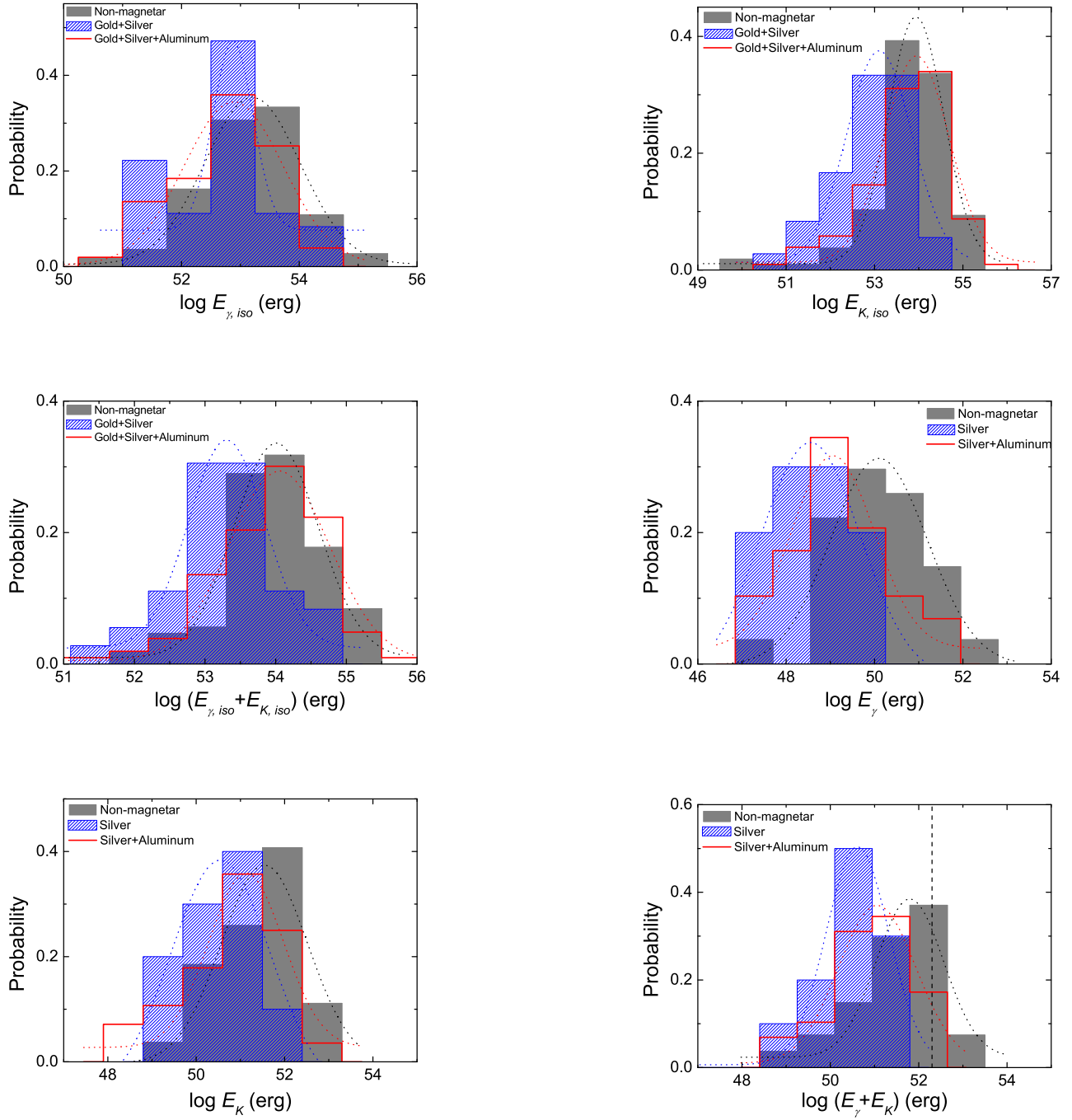


FIG. 9.— Comparisons between the energy histograms of the non-magnetar sample and the magnetar samples. The non-magnetar, Gold+Silver, and Gold+Silver+Aluminum sample histograms are denoted as grey filled, blue hatched, and red open histograms, respectively. Best-fit Gaussian profiles are denoted in black, blue, and red dotted lines, respectively. The six panels denote histograms of $E_{\gamma, iso}$, $E_{K, iso}$, $(E_{\gamma, iso} + E_{K, iso})$, (E_{γ}, E_K) , and $(E_{\gamma} + E_K)$, respectively.

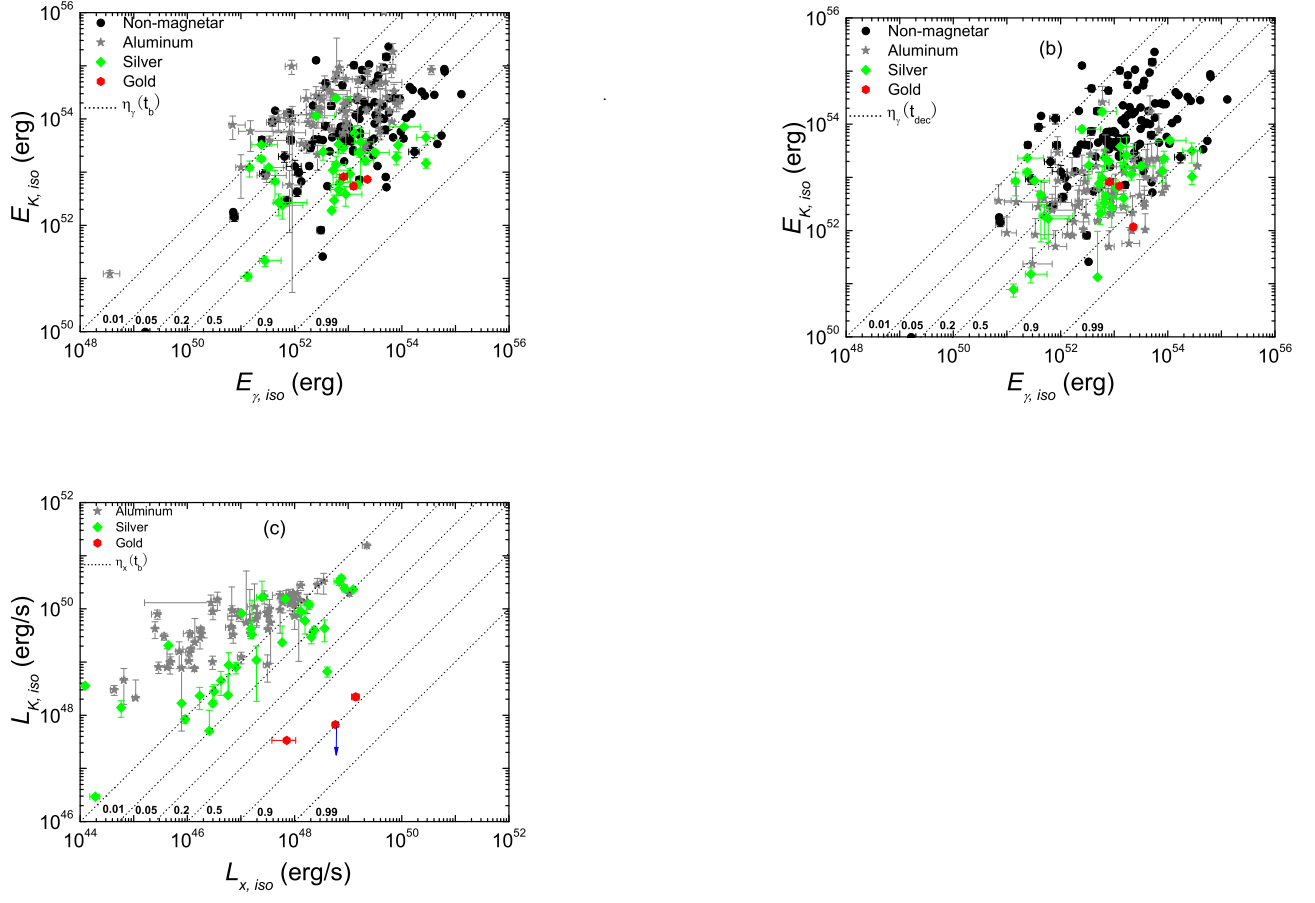


FIG. 10.— (a) The $E_{\gamma, iso} - E_{K, iso}$ scattered plot for all the GRBs with redshift measurements in our samples: Gold (red), Silver (green), Aluminum (grey), and non-magnetar (black). slanted dashed lines mark the constant γ -ray efficiency (η_γ) lines. $E_{K, iso}$ is calculated at t_b ; (b) Same as (a), but with $E_{K, iso}$ calculated at t_{dec} ; (c) The $L_{X, iso} - L_{K, iso}$ scattered plot for the magnetar samples. Gold (red), Silver (green), and Aluminum (grey). The constant X-ray efficiency η_X lines are over plotted. The $L_{X, iso}$ value of silver and aluminum sample GRBs are all upper limits. For one Gold sample GRB, $L_{K, iso}$ is an upper limit (denoted in the figure).

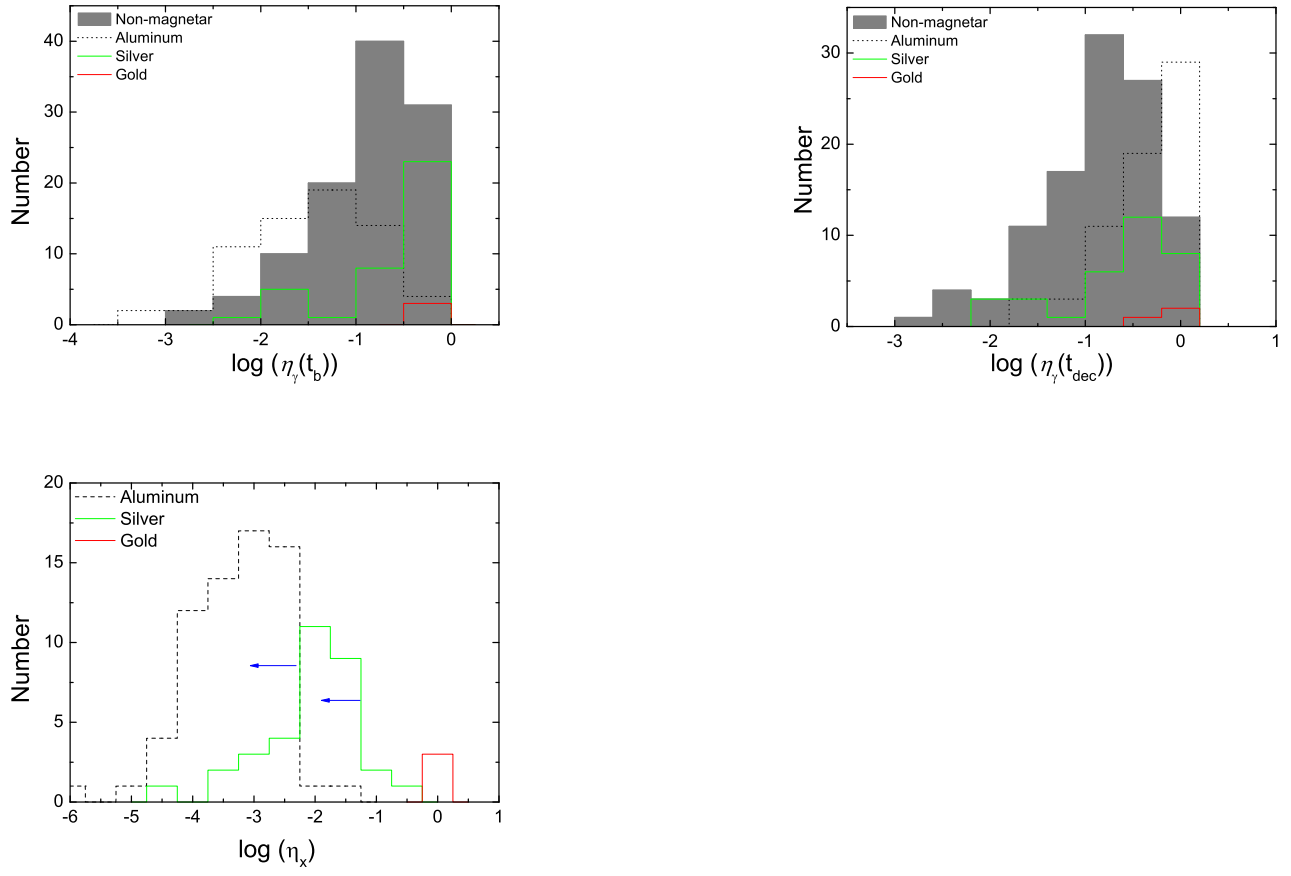


FIG. 11.— Histograms of $\eta_\gamma(t_b)$, $\eta_\gamma(t_{dec})$ and η_X of our samples. For η_X , the silver and aluminum samples only give upper limits.

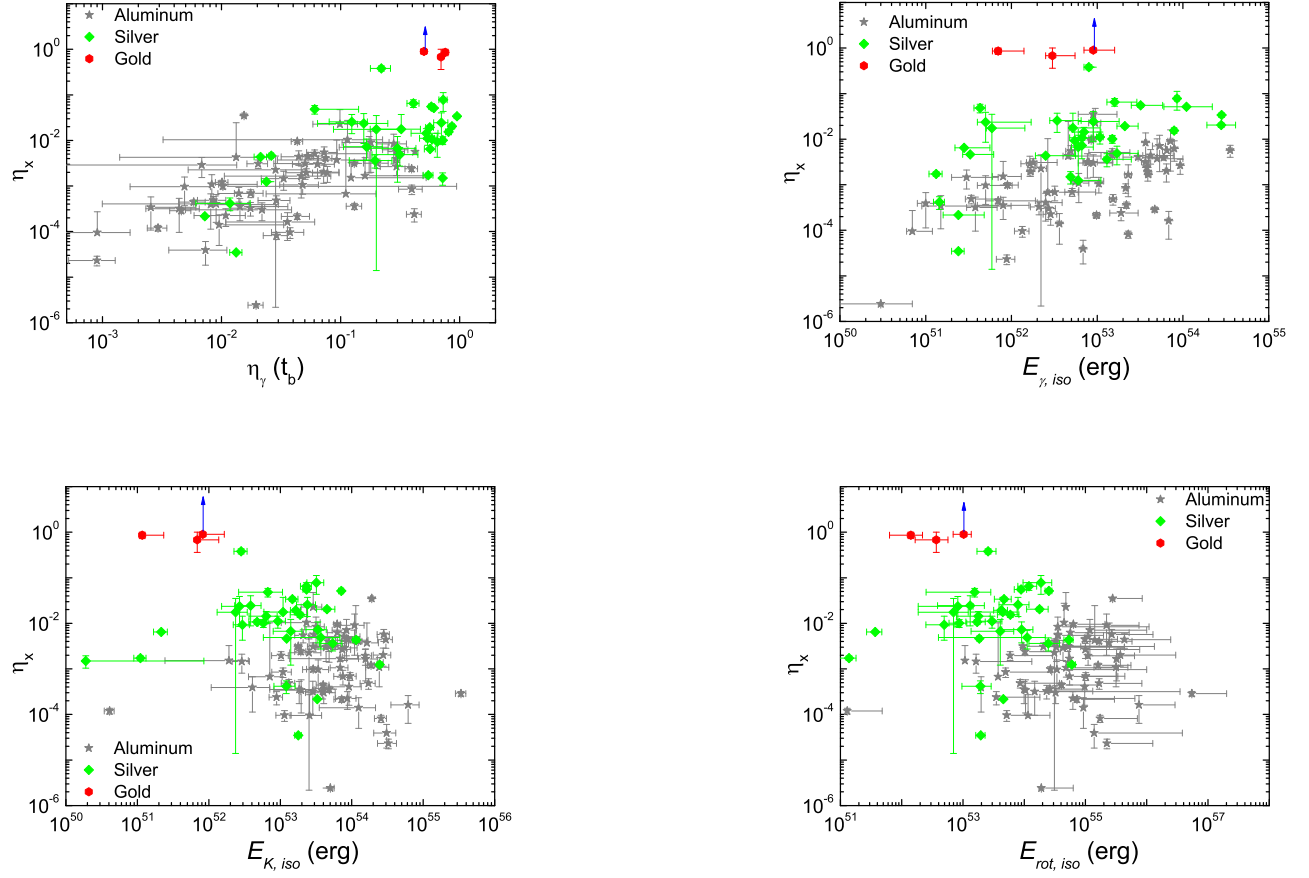


FIG. 12.— The scatter plots of the X-ray efficiency η_X vs. several parameters: $\eta_\gamma(t_b)$, $E_{\gamma, iso}$, $E_{K, iso}$, and E_{rot} . Color conventions are the same as Fig. 5. The η_X values of all Silver and Aluminum sample GRBs are all upper limits. The blue arrow shows the lower limit of one GRB in the Gold sample.